Published in final edited form as:

Curr Biol. 2021 February 22; 31(4): 696–706.e9. doi:10.1016/j.cub.2020.11.010.

Smoothelin-like 2 inhibits Coronin-1B to stabilize the apical actin cortex during epithelial morphogenesis

Mariam Hachimi[1,2], **Catalina Grabowski**[1], **Silvia Campanario**[1], **Gonzalo Herranz**[1], **Gabriel Baonza**[1], **Juan Serrador**[1], **Sergio Gomez-Lopez**[1], **Maria D. Barea**[1], **Minerva Bosch-Fortea**[1,3], **Darren Gilmour**[4,5], **Michel Bagnat**[6], **Alejo E. Rodriguez-Fraticelli**[1,2,*], **Fernando Martin-Belmonte**[1,*,#]

[1]Program of Tissue and Organ Homeostasis, Centro de Biologia Molecular “Severo Ochoa”, CSIC-UAM, Madrid, 28049, SPAIN [2]Present address: Stem Cell Program, Boston Children’s Hospital, Harvard Medical School, Boston, USA [3]Present address: Institute of Bioengineering and School of Engineering and Materials Science, Queen Mary University of London, Mile End Road, London, E1 4NS, UK. [4]European Molecular Biology Laboratory, Heidelberg, 69117, DE. [5]Present address: Institute of Molecular Life Sciences, University of Zurich, Switzerland [6]Dept. of Cell Biology, Duke University, Durham, NC, 27710, US

SUMMARY

The actin cortex is involved in many biological processes and needs to be significantly remodeled during cell differentiation. Developing epithelial cells construct a dense apical actin cortex to carry out their barrier and exchange functions. The apical cortex assembles in response to three-dimensional (3D) extracellular cues, but the regulation of this process during epithelial morphogenesis remains unknown. Here, we describe Smoothelin-like 2 (SMTNL2) function, a member of the smooth-muscle related Smoothelin protein family, in apical cortex maturation. SMTNL2 is induced during the development of multiple epithelial tissues and localizes to the apical and junctional actin cortex in intestinal and kidney epithelial cells. SMTNL2 deficiency leads to membrane herniations in the apical domain of epithelial cells, indicative of cortex abnormalities. We find that SMTNL2 binds to actin filaments and is required to slow down the turnover of apical actin. We also characterize the SMTNL2 proximal interactome and find that SMTNL2 executes its functions partly through inhibition of Coronin-1B. While Coronin-1B-mediated actin dynamics are required for early morphogenesis, its sustained activity is detrimental for the mature apical shape. SMTNL2 binds to Coronin-1B through its N-terminal coiled-coil region and negates its function to stabilize the apical cortex. In sum, our results unveil a

*Correspondence: fmartin@csic.uam.es, alejo.r.fraticelli@gmail.com.
#Lead contact

AUTHOR CONTRIBUTIONS

M.H., A.E.R, and F.M.B designed all experiments. M.H. made mutant lines. M.D.B and M.B. made the transgenic line. S.C., M.H, M.B.F, and T.G conducted cell culture experiments. S.L.G performed Arp2/3 experiments. M.H performed EM and WISH. M.H, and S.C ran RT qPCR. S.C performed WB experiments. M.H performed BioID and IP experiments. A.E.R performed bioinformatic re-analysis. M.H performed the ECIS experiments F.M.B., D.G, and M.B provided reagents and guidance. M.H, A.E.R, and F.M.B. analyzed data and wrote the manuscript. A.E.R. and F.M.B. co-supervised the study and F.M.B. provided the financial support.

DECLARATION OF INTERESTS

The authors declare no competing interests.

mechanism for regulating actin dynamics during epithelial morphogenesis, providing critical insights on the developmental control of the cellular cortex.

INTRODUCTION

All animal cells present a cell cortex, a rich actomyosin meshwork linked to the plasma membrane, responsible for defining their shape (Chalut and Paluch, 2016). Different cell types require unique morphologies to properly carry out their function (i.e., red blood cells, muscle cells, neurons), which rely on specific changes in their actin cortex. In gut morphogenesis, intestinal epithelial cells (IECs) reorganize their apical domain to form a highly polarized actin structure known as the brush border, which is comprised of an array of finger-like membrane protrusions called microvilli, increasing the apical surface for molecular ion exchange (Wallace and Pack, 2003). This brush border generation requires the assembly of a three-dimensional actin cortex localized beneath the apical domain, known as the terminal web. The formation of this specialized actin cortex is essential for the correct physiology of epithelial cells, but the molecular players that trigger this process during morphogenesis remain poorly characterized (Gottlieb et al., 1993; Klingner et al., 2014).

Cortical actin is principally modulated by polymerization factors (Arp2/3 complex and mDia1), motor proteins (Myosins), actin capping, bundling and crosslinking proteins, and membrane-actin linkers (Chugh and Paluch, 2018). Although all of these essential components are conserved between different cell types, cell-specific machinery must contribute to the morphological and functional variation. For instance, the localized activity of two actin-binding proteins, Cortactin and Coronin, establishes a critical balance between Arp2/3-dependent actin branching and actin depolymerization, which regulates cellular shape during migration (Cai et al., 2007a; Cai et al., 2008; Cai et al., 2007b). However, little is known about the genetic control of these actin-regulating proteins during epithelial morphogenesis, leading to the open question of how specialized cortex networks are assembled during this process (Clark et al., 2014).

In the present study, we define the role of Smoothelin-like 2 (SMTNL2) in epithelial morphogenesis. SMTNL2 is the least characterized member of the Smoothelin family of smooth muscle proteins. Smoothelins are defined by a highly conserved calponin homology domain and stabilize actomyosin bundles during smooth muscle differentiation (Bodoor et al., 2011; Borman et al., 2009; Kurita et al., 2004; Lontay et al., 2015; Lontay et al., 2010; Murali and MacDonald, 2018). Here, we unveil the function of SMTNL2, an epithelial Smoothelin, in the process of apical cortex maturation using organotypic three-dimensional (3D) cultures and zebrafish enterocytes as model systems. We propose that SMTNL2 is induced during morphogenesis to stabilize actin dynamics in the apical cortex through the inhibition of Coronin-1B.

RESULTS

SMTNL2 is required for apical cortex integrity in zebrafish enterocytes

Previous studies have demonstrated the existence of a genetic program that is required during lumen morphogenesis in different systems (Alvers et al., 2014; Rodriguez-Fraticelli et al., 2015; Gálvez-Santisteban et al. 2012). We identified SMTNL2 as one of the strongest hits in an RNAi screening, which prompted us to investigate its function *in vivo* further. Using mouse single-cell developmental atlases, we also found that SMTNL2 is expressed during epithelial morphogenesis in multiple organs, including foregut, lung, skin, and kidney (Supplementary Fig. 1a–c) (Cao et al. 2019). We decided to study the function of SMTNL2 in the zebrafish, an easily accessible model to study epithelial morphogenesis, where most epithelial organs are formed at 144 hours post-fertilization (hpf). Using sequence alignment, we found that zebrafish Smtnl is the closest homolog of mammalian SMTNL2 (Supplementary Fig. 1d). We studied Smtnl expression using RNA *in situ* hybridization and found that *smtnl* expression is enriched in the gut tube at 96 and 144 hpf (Fig. 1a, *cldn15la* as a positive control; Alvers et al. 2014, Potter et al. 2010). To determine the subcellular localization of Smtnl protein, we injected Smtnl-GFP mRNA in zebrafish embryos at the one-cell stage. We observed that Smtnl-GFP localizes at the cytoplasm but concentrates at the apical-junctional boundaries in pronephric epithelial cells at 32 hpf (Supplementary Fig. 1e–f). To visualize Smtnl in the gut, we used the QF-QUAS system, taking advantage of a stable transgenic line *Tg(Claudin15la: QF*), allowing specific expression in the gut after 72hpf (Alvers et al. 2014). Smtnl-GFP localizes at the subapical cortex and the cytoplasm of polarized IECs at 144 hpf (Fig. 1b). Together, these results suggest a conserved subcellular localization of Smtnl in tubular epithelial organs.

To determine if Smtnl has a role in epithelial morphogenesis *in vivo*, we generated a mutant zebrafish line using the CRISPR-Cas9 technology (Varshney et al., 2015). We designed three single guide RNAs (sgRNA) against different exons and isolated a mutant allele presenting a 17bp deletion in the Exon2 of the *smtnl* gene (*mh001*), which generates a frame-shift mutation that predicts a truncated protein (Fig. 1c). To further confirm that we generated a null allele, we performed RT-qPCR and analyzed gene expression of *smtnl* and its paralogs (*smtna*, *smtnb*, and *smtnl1*). RT-qPCR revealed that homozygous mutants present non-sense mediated mRNA decay only for the *smtnl* gene (Supplementary Fig. 1g). Next, we analyzed the phenotype of $smtnl^{-/-}$ larval guts using immunofluorescence and electron microscopy. Homozygous $smtnl^{-/-}$ larvae present apical herniations of IECs that bulge into the lumen in the middle-posterior gut region at 144 hpf (Fig. 1d,e,f). These results indicate that Smtnl is expressed during epithelial morphogenesis, localizes at the subapical cortex, and is required for apical membrane integrity in the IECs.

SMTNL2 stabilizes cortical actin in 3D-MDCK cells

To determine the molecular function of SMTNL2, we used the 3D-MDCK model system, which suitably recapitulates many aspects of epithelial morphogenesis *in vitro* (Galvez-Santisteban et al., 2012; Rodriguez-Fraticelli et al., 2015). In 3D-MDCK cells, SMTNL2 localizes at the subapical compartment and the apical junctions, resembling the localization found in zebrafish epithelial tubes (Supplementary Fig. 2a,b and Video 1). This common

pattern of subcellular localization suggested that the role of SMTNL2 in apical cortex maturation might be conserved in vertebrate epithelia. Paralleling the phenotype of *smtnl* mutant fish, silencing of SMTNL2 (SMTNL2-KD) resulted in morphogenetic defects in the apical membrane and lumen, and these defects were rescued by expression of a silencing-resistant human SMTNL2 cDNA (Fig. 2a–c and, Supplementary Fig. 2c–f). Besides, SMTNL2-KD cells also presented deficiencies in apical membrane components, as evidenced by a decrease in the apical membrane glycoprotein Gp135/Podxl and the tight junction protein Claudin-2 (Supplementary Fig. 2g–m). In contrast, protein levels of a "sealing" claudin, Claudin-1, were not affected (Supplementary Fig. 2i,j). Interestingly, expression of "leaky" claudins such as Claudin-2, and Podxl is required for normal lumen formation (Bagnat et al., 2007; Meder et al., 2005), suggesting that SMTNL2 loss affects the expression of essential regulators of epithelial morphogenesis.

The apical herniations observed in *smtnl*$^{-/-}$ IECs and the apical malformations in 3D cultures were reminiscent of defects in the actomyosin cortex integrity, which is a major regulator of cell surface tension and undergoes extensive remodeling during epithelial morphogenesis (Chugh et al., 2017; Zihni et al., 2017). To visualize how the maturation of the actin cortex occurs during morphogenesis, we quantitatively analyzed the actin density in lumen-forming 3D spheroids and compared it with 2D-cultured cells. We observed that apical F-actin concentration increases in 3D cultured cells with time, and correlate with an increase in SMTNL2 mRNA levels (Fig. 2d–f). Subapically localized SMTNL2 overlaps with F-actin, further suggesting that SMTNL2 is associated with cortical actin regulation (Fig. 2g). Next, we synthesized and purified His-tagged SMTNL2 peptides covering different regions of interest (coiled-coil, CC, complex region, CR or calponin-homology, CH) and the full-length SMTNL2 protein (FL), and then we tested their direct binding capacity to F-actin *in vitro*. We found that recombinant SMTNL2 interacted with *in vitro* polymerized F-actin, principally through its C-terminal Calponin homology (CH) domain (Fig. 2h, i, and Supplementary Fig. 3a,b). To test the role of SMTNL2 in the maintenance of apical cortex integrity, we measured F-actin content in SMTNL2-KD epithelial cells and observed a reduction in apical F-actin compared to controls (Fig. 2j,k). This reduction was only apparent at 72h, but not before, suggesting that SMTNL2 plays a role in actin cortex maintenance, and not in its formation. To further investigate this hypothesis, we used a photoactivatable GFP-tagged β-actin construct (PA-GFP-Actin) and found that SMTNL2-KD cells present a 37.7% faster turnover of apical actin compared to controls (Fig. 2l). Together, these results indicate that SMTNL2 regulates the apical actin cortex mainly through maintaining the stability of actin filaments.

To better characterize the role of SMTLN2 in cell cortex regulation, we analyzed the gain of function effect of ectopic SMTNL2 expression. Highly overexpressed SMTNL2 mislocalized to the cortex of the basal domain, inducing a significant increase in F-actin intensity in this site (Fig. 2m and Supplementary Fig. 3c). Upon closer inspection, we detected that the basal membrane of SMTNL2 overexpressing cells was adorned by non-apoptotic blebs (Fig. 2m,n, Supplementary Fig. 3d,e, and Video 2). Blebs are contractile spherical membrane protrusions driven by myosin's activation through the RhoA/ROCK/Myosin Light Chain (MLC) module (Charras et al., 2005; Sahai and Marshall, 2003). SMTNL2-induced bleb formation was reduced upon Blebbistatin (Non-Muscular Myosin II

inhibitor) or Y-27632 (ROCK inhibitor) treatment (Supplementary Fig. 3f–h). Also, SMTNL2 overexpressing cells present an increase in activated (phosphorylated) MLC levels (p-MLC) compared to controls, whereas SMTNL2-KD cells display a small but significant decrease (Supplementary Fig. 3i–j). All these data indicate that SMTNL2 expression is sufficient to induce alterations in the cell cortex in ectopic sites, through the actomyosin pathway. Thus, both depletion or high overexpression of SMTNL2 may lead to the cell cortex's malformations in epithelial cells, highlighting the delicate dynamic balance that the actin cortex requires to function epithelial tissues properly.

SMTNL2 forms part of an apical network of actin regulators required for epithelial morphogenesis.

To characterize the molecular mechanisms associated with the loss and gain-of-function SMTNL2 phenotypes, we devised an *in vivo* biotinylation assay (bioID) of SMTNL2 proximal proteins (Supplementary Fig. 4a) (Roux et al., 2012). First, we verified that the human SMTNL2-bioID fusion protein presented a similar localization to SMTNL2-GFP and that it was able to rescue SMTNL2 deficiency (Supplementary Fig. 4b–d). Then, SMTNL2-bioID cells (or control wild-type cells) were cultured in 3D for 72h, incubated overnight (12h) with biotin, and their lysates were processed in a pull-down assay analyzed by mass spectrometry. The SMTNL2-specific proximal proteome was analyzed with the STRING database (www.string-db.org), including SMTNL2 as a node (Fig. 3a). Gene ontology analysis with EnrichR revealed that the SMTNL2 proximal proteome was significantly enriched in actin cytoskeleton regulators, whereas protein complex prediction analysis with hu.MAP suggested a functional association with the Arp2/3 complex (ARPC4) (Fig. 3b and Supplementary Fig. 4e)(Goley and Welch, 2006; Kuleshov et al., 2016). After ranking the bioID interactome list by peptide abundance, the top three actin-regulatory proteins were Cortactin (CTTN), Coronin-1B (CORO1B), and Transgelin-2 (TAGNL2). In contrast to SMTNL2, these proteins are not induced during epithelial morphogenesis (Supplementary Fig. 4f,g). Although all three proteins localized proximal to SMTNL2, only CORO1B and CTTN co-immunoprecipitated with SMTNL2 (Fig. 3c,d, and Supplementary Fig. 4h–j). We also validated these two interactions by recombinant protein synthesis and pull-down (Figures S4K and S4L). These results suggested that while all these proteins are in close proximity, only SMTNL2, CORO1B, and CTTN may be forming a complex in the apical domain.

Interestingly, CORO1B is an important regulator of actin turnover and has been shown to inhibit CTTN and Arp2/3 activities. CORO1B binding and inhibition of Arp2/3 are negatively regulated by PKC-mediated phosphorylation of its Serine-2 (Cai et al. 2005). To study this regulation, we tested the capacity of SMTNL2 to form a complex with phosphomimetic (S2D) and non-phosphorylatable (S2A) mutants of CORO1B. As expected, S2D-CORO1B showed complete abrogation of Arp2/3 binding (Fig. 3e, left panels). Interestingly, SMTNL2 interacted preferentially with S2D-CORO1B (compared to S2A-CORO1B), and SMTNL2 expression led to a partial decrease of Arp2/3 in precipitated WT-CORO1B complexes, compared to control cells (Fig. 3e). These experiments suggest that SMTNL2 expression may displace Arp2/3 from CORO1B, or otherwise disrupt the CORO1B protein complex, in order to mitigate actin turnover. Next, we studied the binding

of CORO1B or CTTN to recombinant SMTNL2 peptides covering regions of interest (Fig. 2h and Fig. 3f,g). CORO1B preferentially binds to the N-terminal CC region, while CTTN preferentially binds to the disordered CR region, although this happens to a far lesser degree. We hypothesized that the CC domain of SMTNL2 binds and inhibits CORO1B, to prevent fast actin turnover and correctly form mature epithelial cells. To determine the functional implication of this CORO1B-SMNTL2 interaction, we tested the phenotype rescue capacity of the CORO1B-binding-deficient SMTNL2 protein lacking the N-terminal CC domain (ΔCC) compared to the full-length SMTNL2 protein (FL). Although the ΔCC SMNTL2 mutant presented a similar localization compared to full-length SMTNL2, it was unable to rescue the phenotype to the same extent, indicating that CORO1B binding through the CC region critically contributes to SMTNL2 function (Fig. 3k)

SMTNL2 suppresses CORO1B activity and supports CTTN function.

If SMTNL2 indeed suppresses CORO1B to enforce correct epithelial morphogenesis, then excess levels of CORO1B should be detrimental to the epithelial shape. To test this, we evaluated the effect of overexpressing CORO1B in normal lumen formation (Fig. 4a). As controls, we also overexpressed SMTNTL2 or CTTN (the Arp2/3-promoting factor, which antagonizes CORO1B). Overexpression of either CORO1B or CTTN showed basal blebs' formation confirming their involvement in cortical actin regulation (Supplementary Fig. 4m). However, while CTTN and SMTNL2 overexpressing cells formed relatively normal lumens, CORO1B overexpressing cells showed apical blebbing or herniations and significantly disrupts lumen formation, reminiscing SMTNL2-depletion phenotypes (Fig. 4a,b, and Supplementary Fig. 4m, white arrowheads). These results suggest that an excess of CORO1B activity antagonizes epithelial morphogenesis. Remarkably, exogenous expression of SMTNL2 partially rescued normal morphogenesis in CORO1B-overexpressing cysts (Fig. 4c,d). Together, these results suggest that SMTNL2 binds to and antagonizes CORO1B activity, counterbalancing its role in actin debranching and depolymerization to promote the apical actin cortex's stability and correct maturation of the epithelial cells. Finally, we hypothesized that if the SMTNL2 loss-of-function phenotypes could be attributed to increased CORO1B activity and decreased Arp2/3 activity, CTTN-overexpressing lines might be protected from SMTNL2-KD. Indeed, we observed that increasing CTTN expression fully rescued SMTNL2 depletion (Fig. 4e,f). Finally, consistent with the hypothesis that SMTNL2 acts by promoting the branched actin's stability, dose-dependent Arp2/3 inhibition disrupted apical membrane organization, mimicking the SMTNL2-KD phenotypes (Fig. 4g,h). In contrast to CORO1B-overexpression, the Arp2/3-inhibitor phenotype could not be rescued by exogenous SMTNL2-GFP expression, suggesting that SMTNL2 function (just like CORO1B and CTTN) is upstream of this actin-branching machinery and depends on it for its function. Together, these results suggest that SMTNL2 interacts with and inhibits CORO1B to stabilize actin dynamics and maintain the apical actin cortex during epithelial morphogenesis.

DISCUSSION

In the present study, we identify a role for an epithelial Smoothelin, SMTNL2, as a component of the apical and junction cortex required for epithelial morphogenesis.

SMTNL2 carries its function at least in part through binding other actin regulatory proteins in its N-terminal portion, the least conserved region in the Smoothelin-family proteins. Due to the considerable divergence of Smoothelins in the N-region, it is likely that CORO1B and CTTN binding are unique features of SMTNL2. This further highlights the diversification of proteins with Smoothelin-type CH domains through accessory actin regulatory protein modules, resulting in a family of proteins with widely distinct functions that share this conserved domain.

Interestingly, SMTNL2 seems to be the only member of the CORO1B-CTTN-SMTNL2 actin-regulatory module that is induced during epithelial tissue maturation, highlighting its role as a regulator of this process. Our most robust evidence supporting the role of SMTNL2 in actomyosin regulation stems from the observation of bleb phenotypes in both mutant and overexpression contexts (Charras and Paluch, 2008; Charras, 2008; Fackler and Grosse, 2008). Other Smoothelin family members had been previously reported to bind and regulate myosin in smooth muscle (Lontay et al., 2010; Murali and MacDonald, 2018; Turner and MacDonald, 2014; Ulke-Lemee et al., 2014). Despite the changes in MLC phosphorylation upon SMTNL2 modulation (Supplementary Fig. 3i,j), we did not detect any myosins or myosin regulatory proteins in the SMTNL2 interactome, implying that SMTNL2 regulates myosin indirectly through actin polymerization-depolymerization at the cell cortex. Supporting this hypothesis, both CTTN and CORO1B are present in membrane blebs, and we showed that their overexpression results in bleb formation (Bovellan et al., 2014; Charras et al., 2006).

Interestingly, both SMTNL2 overexpression and deficiency resulted in cell cortex abnormalities, emphasizing the delicate balance that maintains membrane structure. In the zebrafish gut, *smtnl* mutants presented defects in apical cortex integrity, resulting in herniations that project into the luminal cavity, disrupting the brush border structure. Studies in chick intestine explants with Cytochalasin-B, a drug that blocks actin polymerization, observed the formation of similar apical herniations (Burgess and Grey, 1974). Furthermore, the knock-out of Ezrin, a cell cortex protein that links actin to the apical membrane proteins, also presents with brush border abnormalities with intestinal apical membrane bulging into the luminal cavity (Casaletto et al., 2011). Thus, our evidence strongly supports that SMTNL2 acts in the same pathway. In our model, apical transmembrane proteins, such as Podxl, and tight junction components, such as claudins and ZO-1, would recruit Ezrin, concomitantly anchor and stabilize the apical actin cortex. During early epithelial development, constant actin remodeling requires fast turnover kinetics.

In comparison, the mature epithelial cortex requires more sturdy and stable actin structures. While this could be achieved simply by turning down CORO1B levels, CORO1B-mediated actin turnover is probably essential in other processes such as endocytosis. The simpler solution that epithelial cells seem to have settled on is to turn up the expression of a CORO1B inhibitor, SMTNL2, which is targeted to the rich F-actin cortex through its CH domain and prevents actin destabilization by blocking CORO1B binding of Arp2/3. The end product of SMTNL2 activity is to create a stable meshwork of branched actin filaments that supports the cortex structure in the apical pole of the cells.

Interestingly, brush border alterations are also observed in either genetic or acquired enteropathologies (Delacour et al., 2016; Wallace et al., 2005). In addition, cell cortex abnormalities and membrane blebbing are hallmarks of highly metastatic malignant cells (Sahai and Marshall, 2003). It will be interesting to measure SMTNL2 expression levels and activity during invasion or migration of tumor cells and determine if SMTNL2 is required for colon carcinoma progression. Future studies of the mechanisms responsible for the apical cortex maturation in zebrafish could be critical for elucidating the molecular basis of congenital gut defects and provide novel insight into intestinal oncogenesis and metastasis (Rubin, 2007; Zhong, 2005).

MATERIALS AND METHODS

Plasmids.

Human TAGNL2-GFP plasmids were kind gifts from Dr. Chang Duk-Jun (Gwangju Institute of Science and Technology, South Korea). Human SMTNL2-GFP and SMTNL2-Cherry were cloned from human cDNA, constructed by PCR and cloned into pEGFP/mCherry vectors (Clontech). Human SMTNL2-myc/myc-birA* was constructed by PCR and cloned into mCherry vector (Clontech), substituting mCherry with the promiscuous mutant of birA* (+). The plasmids containing Smtnl under SP6 promoter and pTol2-QUAS:Smtnl-GFP were constructed by RT-PCR from whole embryo mRNA and Gateway cloning (Invitrogen). The Gateway backbone plasmids were kind gifts from Dr. Gilmour from the EMBL Heidelberg (Germany) and Dr. Michel Bagnat from Duke University (USA). Full-length human pEmerald-CORO1B-N-10 was a gift from Michael Davidson, and mouse GFP-CTTN was a gift of Kenneth Yamada (both plasmids were obtained from Addgene #54050 and #26722).

Antibodies and reagents.

Podocalyxin/gp135 mAb (1:500 IF, 1:1,000 WB) was a gift from G. Ojakian (State University of New York Downstate Medical Center, USA). GAPDH mAb 6C5 (no. sc-32233, 1:1,000 WB, Santa Cruz Biotechnologies), ß-catenin pAb (no. sc-7199, 1:500 IF, Santa Cruz Biotechnologies), GFP mAb (no.11814460001, 1:1,000 WB, 1:1,000 immunoprecipitation (IP) Roche), GFP pAb (no. A-11122, 1:1,000 immunoprecipitation (IP), 1:1,000 IF, 1:2,000 WB, Life Technologies), myc 9E10 mAb (no. 11667149001, 1:1,000 IF on acetone fixation, Roche), RFP pAb (no. PM005, 1:1,000 immunoprecipitation (IP), MBL), Cortactin p80/85 mAb (no. 05–180, clone 4F11, 1:500 IF, MERCK), tubulin (no. T9026, DM1A, 1:1,000 WB, Sigma-Aldrich), pMLC2 pAb (no. 3671, 1:100 IF, 1:500 WB, Cell Signaling Technology), ZO-1 pAb (no.R4076, 1:500 IF, DSHB), Claudin2 pAb (no. 51–6100, 1:500 IF, 1:500 WB, Zymed), cleaved Caspase3 pAb (no. 9661, 1:500 IF, Cell Signaling Technology), were used as primary antibodies. Peroxidase-conjugated antibodies were used for western blotting (Jackson Immunoresearch). Alexa 405/488/555/647-conjugated phalloidin or secondary antibodies and WGA-FITC (Sigma-Aldrich) were used for immunofluorescence. DAPI (10 μg/ml) was from Life Technologies. CK-666 (Sigma-Aldrich) was used at 0–100μM in culture medium for up to 72h to inhibit Arp2/3 (Nolen et al. Nature 2009). Blebbistatin (Sigma-Aldrich) was used at 25μM to inhibit myosin-II activity, and Y-27632 (Sigma-Aldrich) was used at 10μM to inhibit ROCK activity.

Transgenic animals and mutants.

Zebrafish stocks were maintained at 28C°. The zebrafish lines used were AB1, *smtnl*^{mh001}, and *Tg(cldn15la:QF)*. Zebrafish that were found dead, not swimming or without heartbeat were excluded from the analyses. To randomize animal selection, we followed common protocols for unbiased tank fishing (Zfin.org). Genotypes were determined by tail fin clipping and PCR. The QF-QUAS system was used for zebrafish transgenesis (Subedi et al., 2014). For Smtnl-GFP expression analysis in the gut, one-cell stage *Tg(cldn15la:QF)* embryos were injected with linearized and purified pTol2-QUAS:Smtnl-GFP at 0.1 ng per embryo, and 5 dpf larvae were analyzed. Experiments were supervised by the bioethics committee of the Centro de Biología Molecular `Severo Ochoa' (CSIC) and performed in compliance with bioethical regulations of the European Commission. There was no requirement for animal randomization during animal studies.

CRISPR design, assembly, injection, and mutant screening.

An allele consisting of a 17bp deletion in the *smtnl* transcript (NP_997970.1) was generated using CRISPR/Cas9 system targeting the second exon of *smtnl* gene. Cas9 mutagenesis was designed and performed as previously described (Varshney et al., 2015). The targeting site sequence was: 5'-GGCCGAGCCGCTGGCGGAGC-3'. The quality of the assembled oligos was checked on a 1.5% agarose gel. DNA purification was performed with the Min-elute gel extraction kit, and gRNA were synthesized using Megashort T7 mRNA transcription synthesis kit (Thermofisher scientific). Cas9 protein was a purchased gift from Dr. Gilmour. A mix of Cas9 protein (150 ng/ul) and gRNA (30 ng/μL) together with 180mM of KCl was co-injected into one-cell stage WT embryos. To determine mutation efficiency, genomic DNA was extracted from approximately 30-24hpf embryos followed by fluorescent PCR and fragment analysis. Data were analyzed for allele sizes and corresponding peak heights using the local Southern algorithm available in the Genescan and Genotyper software of the GeneMapper software package (Life Technologies). The allele sizes were used to calculate the observed indel mutations. Mutations from two independent founders that were not in multiples of 3 bp and thus predicted to be frameshift truncations were selected for further confirmation by sequencing. Adult F1 progeny of these founder fish were genotyped similarly by fluorescent PCR using DNA extracted from fin clips and finally identified by TOPO cloning (Invitrogen) and Sanger sequencing.

In situ hybridization.—Cldn15la probe was used to detect the zebrafish gut (Alvers et al., 2014). The probe to detect the smtnl transcript by in situ hybridization was PCR amplified from a mix of 24–72 hpf larval cDNA and ligated into pGEMT- Easy (Promega). In situ hybridization was performed as previously described (Bagnat et al., 2007). The plasmids were linearized, and digoxygenin-labelled RNA was generated using the DIG-labelled nucleotides (Roche) and T7 polymerase (NEB) or Sp6 for Cldn15la probe. Stained embryos were imaged on a Discovery.V20 stereoscope (Zeiss) with an Achromat S 1.0 × lens.

Fish sectioning and analysis.

Zebrafish embryos and larvae from different time points were fixed overnight in PBS-buffered 4% PFA (Sigma), washed twice in PBS and embedded in PBS-buffered 4% low-

melt agarose blocks. Blocks were cut in 100 μm sections using a Vibratome (Leica). Sections were blocked/permeabilized with PBS-3% BSA containing 1% Tx100 and then incubated with the indicated antibodies. Stained sections were mounted using Fluoromount. Sectioned fish were analysed on a confocal microscope. Data were repeated using three different sections from the same tissue and/or genotype. Representative images are shown.

Cell culture and stable cell lines.

MDCK type 2 (MDCK-II, MDCK.2) cells were obtained from ATCC and grown as described previously (Galvez-Santisteban et al., 2012). MDCK cells stably expressing SMTNL2-GFP, Cherry-SMTNL2, GFP-CTTN, mEmerald-CORO1B and GFP-TAGNL2 were made by transfection using Lipofectamine 2000 (Life Technologies) and clones were selected by treating cells with G418 (0.5mg ml^{-1}). The double stable cell lines were made by co-transfection with the blasticidin-resistant gene (pBlast) and selection for 10 days with 0.5μg ml^{-1} blasticidin. Mycoplasma testing was regularly performed. To prepare cysts in Matrigel, cells were trypsinized to a single cell suspension of 2×10^4 cells ml^{-1} in 2% Matrigel and plated in coverglass bottom chambers (IBIDI) covered with Matrigel. Cysts were grown and fixed at indicated time points.

Confocal and electron microscopy.

Zeiss laser scanning confocal microscopes LSM510, LSM710, two-photon LSM710 and Nikon AR1+ used for laser scanning confocal imaging. Objectives used were usually 40×/0.95 oil-Plan Apochromat and 63×/1.4 oil-Plan Apochromat (Zeiss). For electron microscopy, 144hpf larvae were fixed in 2% (w/vol) PFA, 2% (w/vol) glutaraldehyde in 0.1 M phosphate buffer at pH 7.4 for 2h at room temperature and overnight at 4°C. Subsequently, midgut sections were embedded in Epon resin, sectioned using an ultramicrotome (Ultracut E, Leica), and stained with uranyl acetate and lead citrate and imaged at 80 kV using a JEM1010 Jeol microscope. For video-microscopy we processed maximum z-projections of all stacks using ImageJ software. Image analysis and composition were performed with ImageJ, Fiji, and/or Zen (Zeiss) programs. For quantifications, more than three experiments were quantified per condition. Significance was calculated using a paired, two-tailed Student’s t-test, and significant p-values are indicated in each experiment.

RNAi and Real-time quantitative PCR.

Twenty-five nucleotide stealth siRNA duplexes targeting specific mRNA sequences of canine SMTNL2, CORO1B, CTTN, and TAGNL2 were designed and purchased from Invitrogen using the Stealth RNAi BLOCK-IT technology. Sequences were submitted to BLAST search to ensure targeting specificity. MDCK cells were transfected by Lipofectamine 2000. Cells were transfected with 10ml of siRNA (20uM) in 6-well plates, cultured for 24h, trypsinized and then plated to grow cysts for the indicated time points. Total cell lysates were analyzed by quantitative real-time PCR (Q-PCR) to confirm siRNA efficiency. For rescue experiments, GFP-tagged human SMTNL2 was verified to be resistant to SMTNL2 siRNA by RT-qPCR. Quantitative analysis of gene expression was carried out by real-time quantitative PCR. RNAs were purified from cells or zebrafish guts using the RNA easy kit (Qiagen) to eliminate genomic DNA contamination. RNA was converted into cDNA using the RNA-to-cDNA High capacity kit, and then qPCR was performed using the

ABI-PRISM 7900HT SDS system (Applied Biosystems). PCRs were performed on 10 ng template cDNA per well using intron-spanning primers. Specificity was BLAST-analysed for each primer pair, and we performed a melting curve analysis to ensure that a single PCR product was generated.

The siRNA targeted the following sequences: control: 5'-GCUGGUCCGGAGGCAUUAAUUGUUA-3' SMTNL2 no.1: 5'-CAGAAUACCCAGGGUUCCUUCCAUU-3' SMTNL2 no.2: 5'-GAGGUAACUGCAUCUGUACUGUUGA-3' CORO1B no.1: 5'-GGCAGAGCAAAUUCCGGCAUGUGUU-3' CORO1B no.2: 5'-CACCCUGACCUCAUCUACAACGUCA-3' CTTN no.1: 5'-GGACAGAGUUGAUCAGUCUGCUGUA-3' CTTN no.2: AAGCGUGAAGCAAGCAGAGAGUGAU-3' TAGNL2 no.1: 5'-GCUGUGGCUGCAGGGACUUAAUUUA-3' TAGNL2 no.2: 5'-UGUGGCUGCAGGGACUUAAUUUAUA-3'

Single cell RNAseq analysis.

Previously published epithelial lineage single cell RNAseq data was downloaded from the following address: https://oncoscape.v3.sttrcancer.org/atlas.gs.washington.edu.mouse.rna/downloads. This dataset contains single cell RNAseq analysis of whole mouse embryos collected at different embryonic days. The counts matrices corresponding to cells of the epithelial lineage were first loaded using Rstudio with the packages Seurat and Monocle, and then exported using the write10xCounts() function. The mtx files were then loaded and analyzed with Scanpy (v1.4.6)(Wolf et al., 2018). Loaded genes were filtered by minimum counts (n=5), and loaded cells were filtered by minimum counts (n=100). Counts were normalized to 10,000 counts per cell, and transformed using the log1p function. Then, highly variable genes were identified and used to compute principal components (number of pca = 50). A neighbor cell map was generated with n_neighbors=20, and the UMAP embedding was computed. Clusters were calculated using the Leiden algorithm (resolution = 0.75). The clusters where Smtnl2 was differentially expressed (adjusted $p<0.05$ in a Benjamini-Hochberg-corrected t-test) were labeled and marked with arrowheads.

Western blot.

Immunoblots shown are representative of experiments that were repeated and reproduced at least three independent times.

Immunoprecipitation.

HEK 293T (10^6 cells) transiently coexpressing GFP-CORO1B or GFP-CTTN with SMTNL2-Cherry were grown for 48 h, washed once in cold PBS and lysed in 1ml of lysis buffer (150mM NaCl, 20mM Tris HCl, pH 8.0, Glycerol 1%) containing 1% NP40 and protease inhibitor cocktail (Sigma-Aldrich). Every 1 ml of lysate was incubated with 2 µg of purified monoclonal anti-GFP (Roche) or 2 µg of monoclonal GAPDH as isotype IgG1 control (Santa Cruz). Monoclonal anti-GFP-coated magnetic beads (#11031 Thermo Fisher Scientific) were washed in lysis buffer 5 times and dried by aspiration. Bound proteins were eluted in 75µl of 2x Laemmli protein-loading buffer (Sigma-Aldrich) and analyzed by

western blotting. We performed experiments at least three independent times to be confident in the experimental reproducibility.

In vivo biotinylation of SMTNL2-proximal proteins.

MDCK cells stably expressing the promiscuous mutant (R118G) of the humanized bacterial biotin-ligase fused to human SMTNL2 (hSMTNL2–myc/myc–birA*) or wild-type MDCK cells (no birA* controls) were incubated with 50 μM biotin for 16h and lysed using 4% SDS. After reducing the SDS concentration to 2%, biotinylated peptides were purified using streptavidin-coated magnetic beads (Genscript). The bioID technique was performed as previously described, and eluted peptides were analyzed by liquid chromatography-tandem mass spectrometry (Triple-TOF) and peptide-mass fingerprinting (MASCOT) at 1% FDR, considering up to 2 biotinylations per peptide, at the Proteomics unit at Centro Nacional de Biotecnología (CSIC)(Roux et al., 2012). To analyze the bioID results, we first generated a ranked list using the MASCOT protein score to rank the uniquely identified proteins. Using this ranked list, we performed gene-set enrichment analysis (http://enrichr.org), GOrilla (http://cbl-gorilla.cs.technion.ac.il/) and STRING (http://string-db.org/).

Measurements and quantifications.

MDCK cysts with a single (or double) actin/Gp135 staining at the interior surface and β-catenin/ actin facing the ECM were identified as normal “single” lumens. We excluded cyst formation experiments that presented lower than 50% normal lumen formation (at 72 h), usually due to poor Matrigel gelification conditions. These experiments were repeated. To randomize cyst or cell counting, we randomly selected fields using low magnification, and then counted or took images at higher magnification for measurements. Immunofluorescence experiments in cell lines were performed at least three independent times and the images shown are representative from samples that were used for quantification. For fluorescence intensity quantification in MDCK cysts, the background was removed using Fiji, projections of single cells were obtained and the fluorescence signal was quantified as integrated density per cell or total cyst volume. To quantify actin signal polarization, the ratio of apical (actin staining facing the lumen) over total or over [total minus apical] signal was measured. At least 10 cysts (approximately 50 cells) were quantified per experiment, a minimum of three experiments per condition. For bleb measurements, cysts containing 80% of the cells with basal blebs (apparent circular shaped breaks in the basolateral actin cortex) were considered as positive, and the percentage of cysts with blebs (over the total number of cysts in a field) was quantified. For electron microscopy quantifications, larvae with apical blebs were considered abnormal (more than one cell presenting apical blebbing and lack of microvilli in a transversal slide was considered as positive). For the microvilli measurements, we quantified the number of microvilli in normal cells versus cells with apical blebs in the same experiment. For all the measurements, the number of independent experiments, the sample size, and the statistical significance is specified in the figure legends. For RT-qPCR experiments, the percentage of remaining mRNA in each knockdown condition was normalized to the HPRT level and represented as a percentage of the control (scramble siRNA) mRNA levels. The significance was calculated using a paired, two-tailed t-test.

Human ACTB cloning in pPICZA

Homo sapiens ACTB cDNA cloned in the pGEM-T Easy Vector (#A1360, Promega) was modified by PCR using the sense primer (GGT ACC ATG CAC CAT CAC CA TCA CCA TGA AAA CCT GTA CTT CCA ATC CAT GGA TGA TGA TAT CGC CGC G) that contains one KpnI restriction site (underlined) and a start codon followed by a 6x histidine-encoding sequence and TEV protease cleavage site; and the AgeI-containing antisense primer ACCGGTCTAGAAGCATTTGCGGTGGAC. The corresponding PCR product was digested with KpnI/AgeI and subcloned in the pPICZA vector (#V19020, Invitrogen) for expression of 6xHis-tagged human β-actin in *Pichia pastoris* yeast. DNA sequencing of the human ACTB construct in pPICZA (pPICZA/h-β -actin) was performed.

Production of recombinant human β-actin from *Pichia pastoris*

Human β-actin was purified from *P. pastoris* X-33 yeast by modification of the protocol previously described in Haitano et al., 2018. In brief, pPICZA/h-β-actin was linearized with SacI (#R0156, New England Biolabs) and *P. pastoris* X-33 transformed with by electroporation using the Gene Pulser™ electroporation system (Bio-Rad). Transformants were selected by grown at 30°C on yeast extract peptone dextrose (YPD) plates containing 100 μg/ml Zeocin (#R25001, Gibco). Cell clones expressing human β-actin were identified by SDSD-PAGE of cell extracts and both Coomassie staining and western blot with anti-5xHis specific Ab (#34660, Quiagen). To produce recombinant human β-actin, *P. pastoris* transformants were revived on YPD solid medium and cells were inoculated into 200 ml buffered minimal medium (BMM) composed of 1.34% yeast nitrogen base without amino acids (#DF0335, Difco) with 0.00004% biotin, 100 mM K_2HPO_4/KH_2PO_4 pH 6 and 1% glycerol and cultured at 30°C, with rotation at 220 rpm for 24 h. Cells were then adjusted to OD_{600} = 1.0–2.0 in 2 l BMM containing 0.00004% biotin and 0.5% methanol, and cultured in six separate 2 l baffled flasks (330 ml culture each) at 30°C, with rotation at 220 rpm, for 3 days; 0,75 % and 1% methanol were added at 24 h and 48 h of culturing, respectively. Cells were pelleted by centrifugation at 5,000 g at 4°C for 15 min; yielding ~10 g wet weight of cells per 1 l culture. Cells were washed once with water and stored at −80°C until use.

For each purification of recombinant human β-actin, 20 g of frozen cells was used, which was resuspended in 30 ml breaking buffer (PBS pH 7.4 containing 0.4 M NaCl, 12 mM imidazole and 1 mM phenylmethylsulfonyl fluoride (PMSF), 1 μg/ml leupeptin and 2 μg/ml pepstatin as protease inhibitors) and passed three times through a French Press (275.8 MPa each pass). The cell lysate was subsequently cleared by centrifugation at 30,000 g at 4°C for 30 min. The supernatant was incubated with 1.25 ml Profinity™ IMAC resin Ni-charged (#1560133, Qiagen-Bio-Rad) at 4°C for 1–2 h. The resin was loaded into an open PD-10 column (#GE17043501, Sigma) and washed first with ice-cold 35 ml binding buffer; then with 35 ml ice-cold G-buffer (5 mM TRIS pH 8, 0.1 mM $CaCl_2$) containing 12 mM imidazole and 0,4 M NaCl; and finally with 35 ml G-buffer containing 12 mM imidazole. 6xHis-tagged β-actin retained in the resin was sequentially eluted with 750 μl 50 mM, 300 mM and 500 mM imidazole in G-buffer, and all the elution fractions containing recombinant β-actin were combined. The eluate was concentrated using an Amicon ultracell 10 kDa cut-off membrane (#UFC801024, Sigma) and the final volume adjusted to 800 μl with ice-cold

G-buffer. The concentration of actin in fractions was determined both by comparison with Coomassie blue-stained 1 μg BSA in SDS-PAGE and by measuring the absorbance at 290 nm using a NanoDrop 2000c spectrophotometer (Thermo Fisher Scientific)

Smoothelin-β-actin pull-down binding assays

Recombinant full length smoothelin and β-actin were assayed for binding activity each other incubating 4 μg of smoothelin with ~10 μg of β-actin linked up aminolink plus coupling agarose resin of the Pierce direct IP kit (#26148, Pierce) and vice versa, in 0.8 ml G-buffer pH 7.5 containing 0.2 mM ATP and 1 mM DTT at 4 °C for 45 min following the manufacturer's instructions. Protein-linked agarose beads were washed tree times in binding buffer, and bound smoothelin and β-actin were eluted by *boiling in Laemmli sample buffer for* analysis by SDS-PAGE and Coomassie blue staining.

F-actin co-sedimentation assays

Actin co-polymerization assay for the study of smoothelin binding to F-actin was performed similarly as previously described (Srivastava and Barber, 2008). Recombinant human β-actin (6 μM) in 100 μl G-buffer containing 0.2 mM ATP and 1 mM DTT was mixed with 10 μg of either full length smoothelin or its corresponding CC, CR or CH domains, and 10x actin polymerization F-buffer (20 mM $MgCl_2$, 1 mM EGTA, 500 mM KCl and 10 mM ATP) was added to a final volume of polymerization reaction of 111 μl and incubated 40 min at 24°C. The reaction mixture was ultracentrifuged in a TL-100 ultracentrifuge (Beckman) at 100,000 g, 24°C for 30 min. Pellet and supernatant fractions were analysed on Coomassie-stained gels.

STAR Methods

RESOURCE AVAILABILITY

Lead Contact—Further information and requests for resources and reagents should be directed to and will be fulfilled by the Lead Contact, Fernando Martin-Belmonte (fmartin@cbm.csic.es).

Materials Availability—Plasmids generated in this study are available from the lead contact (fmartin@cbm.csic.es). The zebrafish line *smtnl*^{mh001} is available from the lead contact (fmartin@cbm.csic.es). Requests for the zebrafish line *Tg(cldn15la:QF)* should be addressed directly to Dr. Michel Bagnat (michel.bagnat@duke.edu).

Data and Code Availability—Raw data is available from the lead contact upon request (fmartin@cbm.csic.es).

EXPERIMENTAL MODEL AND SUBJECT DETAILS

Zebrafish—Zebrafish stocks were maintained at 28C° and housed at the Centro de Biología Molecular "Severo Ochoa" (CSIC) aquatic facilities. The zebrafish lines used were AB1 (wild-type), *smtnl*^{mh001} (generated in this study) and *Tg(cldn15la:QF)*. Zebrafish stocks were obtained from the EMBL aquatics facility (D. Gilmour) and the Duke University aquatics facility (M. Bagnat). Zebrafish that were found dead, not swimming or

without heartbeat were excluded from the analyses. To randomize animal selection, we followed common protocols for unbiased tank fishing (Zfin.org). Animal genotypes were determined by tail fin clipping and genomic PCR. Zebrafish from 2–12 months old were crossed and all fertilized eggs were collected and cultured at 25–28°C. Embryos (12–48 hpf) and hatched larvae from 3–6 days post fertilization (dpf) were euthanized with tricaine (MS222), fixed using 4% PFA and used for experiments. Experiments were supervised by the bioethics committee of the Centro de Biología Molecular "Severo Ochoa" (CSIC) and performed in compliance with bioethical regulations of the European Commission.

Cell lines

MDCK cells.: MDCK type 2 (MDCK-II) cells in this study were obtained from Dr. David Bryant (Beatson Institute, UK) and Dr. Keith Mostov (UCSF, USA), and were not independently validated. MDCK cells are a spontaneously immortalized cell line derived from the distal kidney tubule of a female Cocker Spaniel dog (*Canis familiaris*). MDCK cells were cultured in MEM supplemented with 10%FBS and 5 mM L-glutamine at 37°C and 5% CO_2. Cells were passaged up to 50 times (1:5 to 1:8 dilution, before reaching confluence) using 0.25% Trypsin-EDTA for dissociation (Thermo Fisher Scientific). Cells were frozen with 5% DMSO in culture media and stored in liquid N_2 tanks up to 2 years. MDCK cells stably expressing GFP-SMTNL2, Cherry-SMTNL2, GFP-CTTN, mEmerald-CORO1B and GFP-TAGNL2 were generated by transfection using Lipofectamine 2000 (Life Technologies) and clones were selected by treating cells with G418 (0.5mg ml^{-1}). Double stable cell lines were made by co-transfection of both plasmids together with a blasticidin-resistant cassette (pBlastR) and selection for 10 days with 0.5μg ml^{-1} blasticidin (Thermo Fisher Scientific). Mycoplasma testing was regularly performed by PCR. To prepare 3D-MDCK cultures in Matrigel, cells were trypsinized to a single cell suspension of 2×10^4 cells ml^{-1} in 2% Matrigel and plated in coverglass bottom chambers (IBIDI) fully covered with 100% Matrigel. Cysts were grown and fixed at indicated time points.

293T cells.: HEK293T cells were a gift from Dr. Miguel Alonso (CSIC), and were not independently validated.

METHOD DETAILS

Plasmid construction—Human TAGNL2-GFP plasmids were kind gifts from Dr. Chang Duk-Jun (Gwangju Institute of Science and Technology, South Korea). Human SMTNL2-GFP and SMTNL2-Cherry were cloned from human cDNA, constructed by PCR and cloned into pEGFP/mCherry vectors (Clontech, Takara bio). Human SMTNL2-myc/myc-birA* was constructed by PCR and cloned into mCherry vector (Clontech, Takara bio), substituting mCherry with the promiscuous mutant of birA (bioID). The plasmids containing zebrafish Smtnl under SP6 promoter and pTol2-QUAS:Smtnl-GFP were constructed by RT-PCR from whole embryo mRNA and Gateway cloning using the LR and BP clonase kits (Thermo Fisher Scientific). The Gateway backbone plasmids were kind gifts from Dr. Gilmour (EMBL Heidelberg) and Dr. Michel Bagnat (Duke University, USA). Full-length human pEmerald-CORO1B-N-10 was a gift from Michael Davidson, and mouse GFP-CTTN was a gift of Kenneth Yamada (both plasmids were obtained from Addgene Cat#54050 and #26722).

Immunofluorescence—All incubations were performed at 4°C using a plate rocker. MDCK cysts were fixed with 10% formalin (neutral buffered) for 20 minutes, permeabilized with 0.1% SDS and 0.2% Triton X-100 in PBS, blocked using PBS 3%BSA with 0.2%Triton X-100 for 1h and and stained with the following antibodies or reagents overnight in blocking buffer.

- Podocalyxin/gp135 3F2 mouse monoclonal (1:500, gift from G. Ojakian, State University of New York Downstate Medical Center, USA)
- β-catenin rabbit polyclonal (Cat#sc-7199, 1:500, Santa Cruz Biotechnologies)
- Myc epitope 9E10 mouse monoclonal (Cat#11667149001, 1:1,000, on acetone fixation, Roche)
- Phospho MLC2 rabbit pAb (Cat#3671, 1:100, Cell Signaling Technology)
- ZO-1 rat pAb (Cat#R4076, 1:500, DSHB)
- Claudin-2 rabbit pAb (Cat#51–6100, 1:500, Thermo Fisher Scientific)
- Cleaved Caspase-3 rabbit pAb (Cat#9661, 1:500, Cell Signaling Technology)
- Alexa Fluor-conjugated phalloidin to stain filamentous actin (1:500, Thermo Fisher, different fluor conjugates, see Key Resources Table)
- DAPI to stain nuclei (Cat#62248, 10 μg/ml, Thermo Fisher Scientific)

Primary antibody solutions were removed and cysts were washed 3 times in blocking buffer over 30min. Alexa Fluor-conjugated Secondary antibodies (various donkey polyclonal anti-mouse, anti-rabbit and anti-rat, see Key Resources Table) were diluted in blocking buffer and incubated for at least 2h before washing and mounting.

Western blot—Protein lysates were diluted in 2x Laemmli Sample buffer, sonicated for 10 seconds and boiled at 95° for 5 minutes before loading on polyacrylamide gels for SDS-PAGE. Gels were transferred to PVDF Immobilon P membranes (Millipore-Sigma) by wet-transfer technique at 30V and 4°C in Tris-Glycine-20% Methanol buffer overnight. Membranes were blocked with 5% non-fat dry milk in PBS with 0.05% Tween-20. All antibodies were diluted in blocking buffer and incubated at room temperature in a plate rocker. The list of antibodies is:

- Podocalyxin/gp135 mouse monoclonal (3F2, 1:1,000, gift from G. Ojakian, State University of New York Downstate Medical Center, USA)
- GAPDH mouse monoclonal (Cat#sc-32233, 6C5, 1:1,000, Santa Cruz Biotechnologies)
- GFP mouse monoclonal (Cat#11814460001, 1:1,000, Roche)
- GFP rabbit polyclonal (Cat#A-11122, 1:2,000, Thermo Fisher Scientific)
- RFP rabbit polyclonal (Cat#PM005, 1:1,000, MBL)
- Alpha-tubulin mouse monoclonal (Cat#T9026, DM1A, 1:1,000, Millipore-Sigma)

- pMLC2 rabbit polyclonal (Cat#3671, 1:500, Cell Signaling Technology)
- Claudin-2 rabbit polyclonal (Cat#51–6100, 1:500, Thermo Fisher Scientific)

Peroxidase-conjugated anti-mouse and anti-rabbit IgG antibodies were used for western blotting (Jackson Immunoresearch, see Key Resources Table).

Culture of MDCK cells with inhibitors—CK-666 (Millipore-Sigma, Cat#SML0006) was used at 0–100μM for 72h to inhibit Arp2/3 (Nolen et al. Nature 2009). Blebbistatin (Millipore-Sigma, Cat#B0560) was used at 25μM to inhibit non-muscular Myosin-II activity, and Y-27632 (Millipore-Sigma, Cat#SCM075) was used at 10μM to inhibit ROCK activity. Vehicle (DMSO) was used in all cases as appropriate control.

Zebrafish transgenics and mRNA expression—For mRNA expression, zebrafish Smtnl was cloned into the p3E plasmid from the Tol2 kit (gift from K. Kawakami). Then, Gateway cloning (BP clonase, Cat# 11789020, Thermo Fisher Scientific) was used to combine the p5E-CMV/SP6, pME-EGFP and p3E-Smtnl plasmids. The resulting construct was linearized with NotI (New England Biolabs) and used as a template for in vitro mRNA synthesis (SP6 mMessage mMachine kit, Cat#AM1340, Thermo Fisher Scientific) and 300 pg of purified mRNA was injected into one-cell embryos.

The QF-QUAS system was used for zebrafish transgenesis (Subedi et al., 2014). For Smtnl-GFP expression analysis in the gut, one-cell stage *Tg(cldn15la:QF)* embryos were injected with linearized and purified pTol2-QUAS:Smtnl-GFP at 0.1 ng per embryo, and 5 dpf larvae were analyzed by sectioning and confocal microscopy.

CRISPR design, assembly, injection, and mutant screening—An allele consisting of a 17bp deletion in the *smtnl* transcript (NCBI ID: NP_997970.1) was generated using CRISPR/Cas9 system targeting the second exon of *smtnl* gene. Cas9 mutagenesis was designed and performed as previously described (Varshney et al., 2015). The targeting site was: 5’-GGC CGA GCC GCT GGC GGA GC-3’. The quality of the assembled oligos was checked on a 1.5% agarose gel. DNA purification was performed with the Min-elute gel extraction kit (Cat# 28604, Qiagen), and gRNA was synthesized using MEGAshortscript T7 mRNA transcription synthesis kit (Cat# AM1354, Thermofisher scientific). A mix of recombinant Cas9 protein (150 ng/ul, Cat# M0386M, New England Biolabs) and purified gRNA (30 ng/μL) together with 180mM of KCl was co-injected into one-cell stage WT embryos. To determine mutation efficiency, genomic DNA was extracted from approximately 30 embryos at 24hph, followed by fluorescent PCR and fragment analysis. Data were analyzed for allele sizes and corresponding peak heights using the local Southern algorithm available in the Genescan and Genotyper software of the GeneMapper software package (Cat# 4475073, Thermo Fisher Scientific). The allele sizes were used to calculate the observed indel mutations. Mutations from two independent founders that were not in multiples of 3 bp and thus predicted to be frameshift truncations were selected for further confirmation by sequencing. Adult F1 progeny of these founder fish were genotyped similarly by fluorescent PCR using DNA extracted from fin clips and finally identified by TOPO cloning (Cat# 450641, Thermo Fisher Scientific) and Sanger sequencing.

***In situ* RNA hybridization—**Cldn15la probe was used to detect the zebrafish gut (Alvers et al., 2014). The probe to detect the smtnl transcript by in situ hybridization was PCR amplified from a mix of 24–72 hpf larval cDNA using the following primer pair: 5'-CCT GAC CCG ACA GGT AGA GA-3' and 5'-CAG CCT ATC ACA GCC AGC TT-3'. The resulting product was ligated into pGEM3Z (Promega). The plasmids were linearized, and digoxygenin(DIG)-labelled RNA was generated using the DIG RNA labeling mix (Cat# 11277073910 Roche) and T7 Highscribe kit (Cat#E2040S, New England Biolabs). In situ hybridization was performed as previously described (Bagnat et al., 2007). Staining was performed with anti-Digoxigenin Fab fragments conjugated with alkaline phosphatase (Cat#11093274910, Roche) and colorimetric detection by NBT/BCIP (Cat#11681451001, Roche). Embryos were imaged on a Discovery.V20 stereoscope (Zeiss) with an Achromat S 1.0 × lens.

Fish sectioning and immunofluorescence—Zebrafish embryos and larvae from different time points were fixed overnight in PBS-buffered 4%PFA (Cat# HT501128, Millipore-Sigma), washed twice in PBS and embedded in PBS-buffered 4% low-melt agarose (Cat# 16520050, Thermo Fisher Scientific). Agarose blocks were cut in 100 μm sections using a Vibratome VT1200S (Leica). Sections were blocked/permeabilized with PBS 3%BSA containing 1% Triton X100 and then incubated with the indicated reagents.

- WGA-FITC (Cat#L4895, 1:500, Millipore-Sigma) to stain glycosylated membrane proteins
- Phalloidin to stain filamentous actin (different fluor conjugates, see Key Resources Table, 1:500, Thermo Fisher Scientific)
- DAPI to stain nuclei (10 μg/ml, Cat# 62248, Thermo Fisher Scientific)
- Acetylated tubulin (Cat# T7451, clone 6–11-B1, 1:1000, Millipore-Sigma)

Stained sections were mounted over a glass slide using Fluoromount (Cat# F4680–25ML, Millipore-Sigma). Sectioned fish were analysed on a confocal microscope. Data were repeated using three different sections from the same tissue and/or genotype. Representative images are shown.

Cell culture and stable cell lines—MDCK type 2 (MDCK-II) cells were grown as described previously (Galvez-Santisteban et al., 2012). MDCK cells stably expressing SMTNL2-GFP, Cherry-SMTNL2, GFP-CTTN, mEmerald-CORO1B and GFP-TAGNL2 were made by transfection using Lipofectamine 2000 (Cat# 11668019, Thermo Fisher Scientific) and clones were selected by treating cells with 0.5mg ml^{-1} G418 (Cat# A1720, Millipore-Sigma). The double stable cell lines were made by co-transfection with the blasticidin-resistant gene (pBlast) and selection for 10 days with 0.5μg ml^{-1} blasticidin (Cat# A1113903, Thermo Fisher Scientific). Mycoplasma testing was regularly performed. To prepare cysts, μslide coverglass bottom chambers (Cat# 80827, IBIDI) were precovered with 20 μl 100% Matrigel (Cat# 354234, BD biosciences) and allowed to solidify at room temperature for 30 minutes. Cells were trypsinized to a single cell suspension of 2×10^4 cells ml^{-1} in 2% Matrigel and plated in the chambers (approximately 250μl per chamber).

Cysts were grown using normal MDCK culture conditions and fixed at indicated time points.

Confocal and electron microscopy—Zeiss laser scanning confocal microscopes (LSM510, LSM710, two-photon LSM710) and Nikon AR1+ confocal microscopes were used for laser scanning confocal imaging. Objectives used were usually 40×/0.95 oil-Plan Apochromat and 63×/1.4 oil-Plan Apochromat (Zeiss). For video-microscopy, processed maximum z-projections of all stacks using ImageJ software. For photoactivation, Image analysis and composition were performed with ImageJ, Fiji, and/or Zen (Zeiss) programs.

Electron microscopy—For electron microscopy, 144hpf zebrafish larvae or 72h MDCK cysts were fixed in 2% (w/vol) PFA, 2% (w/vol) glutaraldehyde in 0.1M phosphate buffer at pH 7.4 for 2h at room temperature and overnight at 4°C. Subsequently, samples were embedded in Epon resin, sectioned using an ultramicrotome (Ultracut E, Leica), stained with uranyl acetate and lead citrate and imaged at 80 kV using a JEM1010 Jeol microscope (Jeol Ltd.).

RNAi and Real-time quantitative PCR—To perform transient expression interference, twenty-five nucleotide stealth siRNA duplexes targeting specific mRNA sequences of canine SMTNL2, CORO1B, CTTN, and TAGNL2 were designed and purchased from Thermo Fisher Scientific using the Stealth RNAi BLOCK-IT technology. Sequences were submitted to BLAST search to ensure targeting specificity. MDCK cells were transfected by Lipofectamine 2000 (Thermo Fischer Scientific). Cells were transfected with 10ml of siRNA (20uM) in 6-well plates, cultured for 24h, trypsinized and then plated to grow cysts for the indicated time points. Total cell lysates were analyzed by quantitative real-time PCR (qPCR) to confirm siRNA efficiency. For rescue experiments, GFP-tagged human SMTNL2 was verified to be resistant to SMTNL2 siRNA by RT-qPCR. Quantitative analysis of gene expression was carried out by real-time quantitative PCR. RNAs were purified from cells or zebrafish guts using the RNeasy kit (Cat# 74104, Qiagen) to eliminate genomic DNA contamination. RNA was converted into cDNA using the RNA-to-cDNA High capacity kit (Cat# 4387406, Thermo Fisher Scientific), and then qPCR was performed using SYBR PCR master mix (Cat#4309155, Thermo Fisher Scientific) and the ABI-PRISM 7900HT SDS system (Applied Biosystems). PCRs were performed on 10 ng template cDNA per well using intron-spanning primers, to avoid genomic DNA amplification. Specificity was BLAST-analysed for each primer pair, and we performed a melting curve analysis to ensure that a single PCR product of adequate melting temperature was generated at the end of the assay.

The siRNA targeted the following sequences: control: 5’-GCU GGU CCG GAG GCA UUA AUU GUU A-3’; SMTNL2 no.1: 5’-CAG AAU ACC CAG GGU UCC UUC CAU U-3’; SMTNL2 no.2: 5’-GAG GUA ACU GCA UCU GUA CUG UUG A-3’; CORO1B no.1: 5’-GGC AGA GCA AAU UCC GGC AUG UGU U-3’; CORO1B no.2: 5’-CAC CCU GAC CUC AUC UAC AAC GUC A-3’; CTTN no.1: 5’-GGA CAG AGU UGA UCA GUC UGC UGU A-3’; CTTN no.2: AAG CGU GAA GCA AGC AGA GAG UGA U-3’; TAGNL2 no.1: 5’- GCU GUG GCU GCA GGG ACU UAA UUU A-3’; TAGNL2 no.2: 5’-UGU GGC UGC AGG GAC UUA AUU UAU A-3’.

Single cell RNAseq analysis—Previously published epithelial lineage single cell RNAseq data was downloaded from the following address: https://oncoscape.v3.sttrcancer.org/atlas.gs.washington.edu.mouse.rna/downloads. This dataset contains single cell RNAseq analysis of whole mouse embryos collected at different embryonic days. The counts matrices corresponding to cells of the epithelial lineage were first loaded using Rstudio with the packages Seurat and Monocle, and then exported using the write10xCounts() function. The mtx files were then loaded and analyzed with Scanpy (v1.4.6)(Wolf et al., 2018). Loaded genes were filtered by minimum counts (n=5), and loaded cells were filtered by minimum counts (n=100). Counts were normalized to 10,000 counts per cell, and transformed using the log1p function. Then, highly variable genes were identified and used to compute principal components (number of pca = 50). A neighbor cell map was generated with n_neighbors=20, and the UMAP embedding was computed. Clusters were calculated using the Leiden algorithm (resolution = 0.75). The clusters where Smtnl2 was differentially expressed (adjusted $p<0.05$ in a Benjamini-Hochberg-corrected t-test) were labeled and marked with arrowheads.

Immunoprecipitation—HEK 293T (10^6 cells) were transiently transfected with Lipofectamine 2000 (Thermo Fisher Scientific). Cells expressing GFP-TAGLN2, GFP-CORO1B or GFP-CTTN together with SMTNL2-mCherry were grown for 48 h, washed once in cold PBS and lysed in 1ml of lysis buffer (150mM NaCl, 20mM Tris HCl, pH 8.0, Glycerol 1%) containing 1% NP40 and protease inhibitor cocktail (Cat# P8340, Millipore-Sigma). Every 1 ml of lysate was incubated with 2 μg of purified monoclonal anti-GFP (Cat# 11814460001, Millipore-Sigma) or 2 μg of monoclonal GAPDH as isotype IgG1 control (Cat# sc-32233, Santa Cruz Biotechnology). Monoclonal anti-GFP-coated anti-mouse IgG magnetic beads (Cat#11031 Thermo Fisher Scientific) were washed in lysis buffer 5 times and dried by aspiration. Bound proteins were eluted in 75μl of 2x Laemmli protein-loading buffer (Millipore-Sigma) and analyzed by western blotting. We performed experiments at least three independent times to be confident in the experimental reproducibility.

***In vivo* biotinylation of SMTNL2-proximal proteins—**The bioID technique was performed as previously described (Roux et al., 2012, Rodriguez-Fraticelli et al. 2015). MDCK cells stably expressing the promiscuous mutant (R118G) of the humanized bacterial biotin-ligase fused to human SMTNL2 (hSMTNL2–myc/myc–birA*) or wild-type MDCK cells (no birA* controls) were incubated with 50 μM biotin for 16h and lysed using 4% SDS and sonicated. After reducing the SDS concentration to 2%, biotinylated peptides were purified using streptavidin-coated Magbeads (Cat# L00424, Genscript). Eluted peptides were analyzed by liquid chromatography-tandem mass spectrometry (Triple-TOF) and peptide-mass fingerprinting (MASCOT) at 1% FDR, considering up to 2 biotinylations per peptide, at the Proteomics unit at Centro Nacional de Biotecnología (CNB-CSIC). To analyze the bioID results, we first generated a ranked list using the MASCOT protein score to rank the uniquely identified proteins. Using this ranked list, we performed gene-set enrichment analysis (http://enrichr.org), GOrilla (http://cbl-gorilla.cs.technion.ac.il/) and STRING (http://string-db.org/).

Human ACTB cloning in pPICZA—Homo sapiens ACTB cDNA cloned in the pGEM-T Easy Vector (Cat# A1360, Promega) was modified by PCR using the sense primer (5'-GGT ACC ATG CAC CAT CAC CA TCA CCA TGA AAA CCT GTA CTT CCA ATC CAT GGA TGA TGA TAT CGC CGC G-3') that contains one KpnI restriction site (underlined) and a start codon followed by a 6x histidine-encoding sequence and TEV protease cleavage site; and the AgeI-containing antisense primer 5'-ACC GGT CTA GAA GCA TTT GCG GTG GAC-3'. The corresponding PCR product was digested with KpnI/AgeI and subcloned in the pPICZA vector (Cat# V19020, Invitrogen) for expression of 6xHis-tagged human β-actin in *Pichia pastoris* yeast. DNA sequencing of the human ACTB construct in pPICZA (pPICZA/h-β -actin) was performed.

Production of recombinant human β-actin from *Pichia pastoris*—Human β-actin was purified from *P. pastoris* X-33 yeast by modification of the protocol previously described in Hatano et al., 2018. In brief, pPICZA/h-β-actin was linearized with SacI (Cat# R0156, New England Biolabs) and *P. pastoris* X-33 transformed with by electroporation using the Gene Pulser™ electroporation system (Bio-Rad). Transformants were selected by grown at 30°C on yeast extract peptone dextrose (YPD) plates containing 100 μg/ml Zeocin (Cat# R25001, Thermo Fisher Scientific). Cell clones expressing human β-actin were identified by SDS-PAGE of cell extracts and both Coomassie staining and Western blot with Penta-His specific antibody (Cat#34660, Qiagen). To produce recombinant human β-actin, *P. pastoris* transformants were revived on YPD solid medium and cells were inoculated into 200 ml buffered minimal medium (BMM) composed of 1.34% yeast nitrogen base without amino acids (Cat# DF0335, Difco) with 0.00004% biotin, 100 mM K_2HPO_4/KH_2PO_4 pH 6 and 1% glycerol and cultured at 30°C, with rotation at 220 rpm for 24 h. Cells were then adjusted to OD_{600} = 1.0–2.0 in 2 l BMM containing 0.00004% biotin and 0.5% methanol, and cultured in six separate 2 l baffled flasks (330 ml culture each) at 30°C, with rotation at 220 rpm, for 3 days; 0,75 % and 1% methanol were added at 24 h and 48 h of culturing, respectively. Cells were pelleted by centrifugation at 5,000 g at 4°C for 15 min; yielding ~10 g wet weight of cells per 1 l culture. Cells were washed once with water and stored at −80°C until use.

For each purification of recombinant human β-actin, 20 g of frozen cells was used, which was resuspended in 30 ml breaking buffer (PBS pH 7.4 containing 0.4 M NaCl, 12 mM imidazole and 1 mM phenylmethylsulfonyl fluoride (PMSF), 1 μg/ml leupeptin and 2 μg/ml pepstatin as protease inhibitors) and passed three times through a French Press (275.8 MPa each pass). The cell lysate was subsequently cleared by centrifugation at 30,000 g at 4°C for 30 min. The supernatant was incubated with 1.25 ml Profinity™ IMAC resin Ni-charged (Cat# 1560133, Bio-Rad) at 4°C for 1–2 h. The resin was loaded into an open PD-10 column (Cat# GE17043501, Miillipore-Sigma) and washed first with ice-cold 35 ml binding buffer; then with 35 ml ice-cold G-buffer (5 mM TRIS pH 8, 0.1 mM $CaCl_2$) containing 12 mM imidazole and 0,4 M NaCl; and finally with 35 ml G-buffer containing 12 mM imidazole. 6xHis-tagged β-actin retained in the resin was sequentially eluted with 750 μl 50 mM, 300 mM and 500 mM imidazole in G-buffer, and all the elution fractions containing recombinant β-actin were combined. The eluate was concentrated using an Amicon Ultracell 10 kDa cut-off membrane (Cat# UFC801024, Millipore-Sigma) and the final volume adjusted to 800 μl

with ice-cold G-buffer. The concentration of actin in fractions was determined both by comparison with Coomassie blue-stained 1 μg BSA in SDS-PAGE and by measuring the absorbance at 290 nm using a NanoDrop 2000c spectrophotometer (Thermo Fisher Scientific).

SMTNL2-β-actin pull-down binding assays—Recombinant full length SMTNL2 binding to β-actin was assayed by pull-down using the Pierce direct IP kit (Cat# 26148, Thermo Fisher Scientific). 4 μg of SMTNL2 was linked to the agarose resin using the aminolink plus reagent, and then incubated with ~10 μg of purified β-actin in 0.8 ml G-buffer pH 7.5 containing 0.2 mM ATP and 1 mM DTT at 4 °C for 45 min following the manufacturer's instructions. Protein-linked agarose beads were washed tree times in binding buffer, and bound actin was eluted by boiling in Laemmli sample buffer for analysis by SDS-PAGE and Coomassie blue staining. The reverse experiment was performed by aminolinking the β-actin and incubating the linked resin with soluble SMTNL2.

F-actin co-sedimentation assays—Actin co-polymerization assay for the study of SMTNL2 binding to F-actin was performed as previously described (Srivastava and Barber, 2008). Recombinant human β-actin (6 μM) in 100 μl G-buffer containing 0.2 mM ATP and 1 mM DTT was mixed with 10 μg of either full length SMTNL2 or its corresponding CC, CR or CH regions, and 10x actin polymerization F-buffer (20 mM $MgCl_2$, 1 mM EGTA, 500 mM KCl and 10 mM ATP) was added to a final volume of polymerization reaction of 111 μl and incubated 40 min at 24°C. The reaction mixture was ultracentrifuged in a TL-100 ultracentrifuge (Beckman) at 100,000 g, 24°C for 30 min. Pellet and supernatant fractions were analysed on Coomassie-stained gels.

QUANTIFICATION AND STATISTICAL ANALYSIS

MDCK cysts with a circular single or double actin/Gp135 staining at the interior were identified as "normal lumens". We did not quantify cyst formation experiments that presented lower than 50% normal lumen formation at 72 h in the control treatment, as this was usually due to poor Matrigel gelification conditions. In these cases experiments were repeated with a different Matrigel batch. To randomize cyst or cell counting, we randomly selected fields using low magnification, and then captured images at higher magnification for measurements. For counting normal lumen formation, at least 100 cysts were counted per experiment and the percentage of normal cysts is reported in each replicate. Immunofluorescence experiments in cell lines were performed independently at least three times (this is precisely indicated in each figure legend). Images shown are representative from samples that were used for quantification.

Fluorescence intensity quantification was performed in Fiji (Image J v.2.1.0). The background was subtracted, total projections of single cells were obtained and the fluorescence signal was quantified as integrated density. To quantify actin polarization, the ratio of apical mean intensity over total mean intensity was measured. The apical region of interest was drawn by hand. At least 10 cysts were quantified per experiment, a minimum of three experiments per condition.

For MDCK cyst electron microscopy, we processed images with Fiji to draw the shape of the largest central lumen using the apical plasma membrane (i.e. the point of attachment of the microvilli) as the periphery. The obtained region of interest was then analyzed with the Measure tool to obtain the circularity value.

For bleb measurements, cysts containing over 50% of the overexpressing cells with basal blebs (apparent circular shaped breaks in the basolateral actin cortex) were considered as positive. The percentage of cysts with blebs (over the total number of cysts in a field) is reported per sample.

For zebrafish experiments, larvae that appeared lethargic, dead or did not have an inflated swim bladder were excluded from analysis. For electron microscopy quantifications, we inspected at least 3 sections for each larva. We report the % of larvae with at least one enterocyte showing apical blebbing.

For RT-qPCR experiments, the percentage of remaining mRNA in each knockdown condition was normalized to the HPRT Ct values and represented as relative change over the control (scramble siRNA-transfected) mRNA levels.

For all quantitative experiments, the number of independent experiments, the sample size, and the p-values are specified in the figure legends. No tests were used to estimate statistical power and no preliminary analysis was used to estimate sample sizes *a priori*. In experiments with small sample size, normality was tested by Shapiro-Wilk test. In experiments with large sample sizes, normality was tested by Kolmogorov-Smirnov. The significance level was established *a priori* at 0.05. Two-tailed paired (control vs. treatment) t-tests were used for comparing sample distributions. One-sample t-tests were used for experiments in which values were normalized to the control treatment.

Supplementary Material

Refer to Web version on PubMed Central for supplementary material.

ACKNOWLEDGMENTS

We thank C. M. Ruiz-Jarabo for her comments on the manuscript. We thank members of the Martin-Belmonte laboratory, Bagnat and Gilmour laboratories for helpful discussions. We thank Viviana Gallardo for helping in the CRISPR design and screening (CBMSO). We thank Jaime Millan and Diego Garcia Weber for the ECIS device (CBMSO). We also thank M. Guerra at the EM Unit for skillful technical assistance. Finally, we thank the Confocal Microscopy unit for technical assistance. This work was supported by grants from the MINECO (BFU2011-22622) and CONSOLIDER (CSD2009-00016) to F.M.B.

REFERENCES

Alvers AL, Ryan S, Scherz PJ, Huisken J, and Bagnat M (2014). Single continuous lumen formation in the zebrafish gut is mediated by smoothened-dependent tissue remodeling. Development 141, 1110–1119. [PubMed: 24504339]

Bagnat M, Cheung ID, Mostov KE, and Stainier DY (2007). Genetic control of single lumen formation in the zebrafish gut. Nature cell biology 9, 954–960. [PubMed: 17632505]

Bodoor K, Lontay B, Safi R, Weitzel DH, Loiselle D, Wei Z, Lengyel S, McDonnell DP, and Haystead TA (2011). Smoothelin-like 1 protein is a bifunctional regulator of the progesterone receptor during pregnancy. The Journal of biological chemistry 286, 31839–31851. [PubMed: 21771785]

Borman MA, Freed TA, Haystead TA, and Macdonald JA (2009). The role of the calponin homology domain of smoothelin-like 1 (SMTNL1) in myosin phosphatase inhibition and smooth muscle contraction. Molecular and cellular biochemistry 327, 93–100. [PubMed: 19219534]

Bovellan M, Romeo Y, Biro M, Boden A, Chugh P, Yonis A, Vaghela M, Fritzsche M, Moulding D, Thorogate R, et al. (2014). Cellular control of cortical actin nucleation. Current biology : CB 24, 1628–1635. [PubMed: 25017211]

Burgess DR, and Grey RD (1974). Alterations in morphology of developing microvilli elicited by cytochalasin B. Studies of embryonic chick intestine in organ culture. The Journal of cell biology 62, 566–574. [PubMed: 4426920]

Cai L, Holoweckyj N, Schaller MD, & Bear JE (2005). Phosphorylation of coronin 1B by protein kinase C regulates interaction with Arp2/3 and cell motility. The Journal of biological chemistry, 280(36), 31913–31923. [PubMed: 16027158]

Cai L, Makhov AM, and Bear JE (2007a). F-actin binding is essential for coronin 1B function in vivo. Journal of cell science 120, 1779–1790. [PubMed: 17456547]

Cai L, Makhov AM, Schafer DA, and Bear JE (2008). Coronin 1B antagonizes cortactin and remodels Arp2/3-containing actin branches in lamellipodia. Cell 134, 828–842. [PubMed: 18775315]

Cai L, Marshall TW, Uetrecht AC, Schafer DA, and Bear JE (2007b). Coronin 1B coordinates Arp2/3 complex and cofilin activities at the leading edge. Cell 128, 915–929. [PubMed: 17350576]

Cao J, Spielmann M, Qiu X et al. The single-cell transcriptional landscape of mammalian organogenesis. Nature 566, 496–502 (2019). [PubMed: 30787437]

Casaletto JB, Saotome I, Curto M, and McClatchey AI (2011). Ezrin-mediated apical integrity is required for intestinal homeostasis. Proceedings of the National Academy of Sciences of the United States of America 108, 11924–11929. [PubMed: 21730140]

Chalut KJ, and Paluch EK (2016). The Actin Cortex: A Bridge between Cell Shape and Function. Developmental Cell 38, 571–573. [PubMed: 27676427]

Charras G, and Paluch E (2008). Blebs lead the way: how to migrate without lamellipodia. Nature reviews Molecular cell biology 9, 730–736. [PubMed: 18628785]

Charras GT (2008). A short history of blebbing. Journal of microscopy 231, 466–478. [PubMed: 18755002]

Charras GT, Hu CK, Coughlin M, and Mitchison TJ (2006). Reassembly of contractile actin cortex in cell blebs. The Journal of cell biology 175, 477–490. [PubMed: 17088428]

Chugh P Clark AG, Smith MB, Cassani DAD, Dierkes K, Ragab A, Roux PP, Charras G, Salbreux G, Paluch EK (2017). Actin cortex architecture regulates cell surface tension. Nature cell biology 19, 689–697. [PubMed: 28530659]

Chugh P, and Paluch EK (2018). The actin cortex at a glance. Journal of Cell Science 131, jcs186254. [PubMed: 30026344]

Clark AG, Wartlick O, Salbreux G, and Paluch EK (2014). Stresses at the Cell Surface during Animal Cell Morphogenesis. Current Biology 24, 484–494. [PubMed: 24560571]

Coravos JS, Mason FM, and Martin AC (2017). Actomyosin Pulsing in Tissue Integrity Maintenance during Morphogenesis. Trends in cell biology 27, 276–283. [PubMed: 27989655]

Delacour D, Salomon J, Robine S, and Louvard D (2016). Plasticity of the brush border - the yin and yang of intestinal homeostasis. Nature reviews Gastroenterology & hepatology 13, 161–174. [PubMed: 26837713]

Fackler OT, and Grosse R (2008). Cell motility through plasma membrane blebbing. The Journal of cell biology 181, 879–884. [PubMed: 18541702]

Galvez-Santisteban M, Rodriguez-Fraticelli AE, Bryant DM, Vergarajauregui S, Yasuda T, Banon-Rodriguez I, Bernascone I, Datta A, Spivak N, Young K, et al. (2012). Synaptotagmin-like proteins control the formation of a single apical membrane domain in epithelial cells. Nature cell biology 14, 838–849. [PubMed: 22820376]

Goley ED, and Welch MD (2006). The ARP2/3 complex: an actin nucleator comes of age. Nature reviews Molecular cell biology 7, 713–726. [PubMed: 16990851]

Gottlieb TA, Ivanov IE, Adesnik M, and Sabatini DD (1993). Actin microfilaments play a critical role in endocytosis at the apical but not the basolateral surface of polarized epithelial cells. The Journal of cell biology 120, 695–710. [PubMed: 8381123]

Hatano T, Alioto S, Roscioli E, Palani S, Clarke ST, Kamnev A, Hernandez-Fernaud JR, Sivashanmugam L, Chapa-Y-Lazo B, Jones A, Robinson RC, Sampath K, Mishima M, McAinsh AD, Goode BL, & Balasubramanian MK (2018). Rapid production of pure recombinant actin isoforms in Pichia pastoris. Journal of cell science, 131(8), jcs213827. [PubMed: 29535210]

Klingner C, Cherian AV, Fels J, Diesinger PM, Aufschnaiter R, Maghelli N, Keil T, Beck G, Tolic-Norrelykke IM, Bathe M, et al. (2014). Isotropic actomyosin dynamics promote organization of the apical cell cortex in epithelial cells. The Journal of cell biology 207, 107–121. [PubMed: 25313407]

Kuleshov MV, Jones MR, Rouillard AD, Fernandez NF, Duan Q, Wang Z, Koplev S, Jenkins SL, Jagodnik KM, Lachmann A, et al. (2016). Enrichr: a comprehensive gene set enrichment analysis web server 2016 update. Nucleic Acids Res 44, W90–97. [PubMed: 27141961]

Kurita R, Tabata Y, Sagara H, Arai K, and Watanabe S (2004). A novel smoothelin-like, actin-binding protein required for choroidal fissure closure in zebrafish. Biochemical and biophysical research communications 313, 1092–1100. [PubMed: 14706655]

Lemke SB, and Schnorrer F (2017). Mechanical forces during muscle development. Mechanisms of development 144, 92–101. [PubMed: 27913119]

Lontay B, Bodoor K, Sipos A, Weitzel DH, Loiselle D, Safi R, Zheng D, Devente J, Hickner RC, McDonnell DP, et al. (2015). Pregnancy and Smoothelin-like Protein 1 (SMTNL1) Deletion Promote the Switching of Skeletal Muscle to a Glycolytic Phenotype in Human and Mice. The Journal of biological chemistry 290, 17985–17998. [PubMed: 26048986]

Lontay B, Bodoor K, Weitzel DH, Loiselle D, Fortner C, Lengyel S, Zheng D, Devente J, Hickner R, and Haystead TA (2010). Smoothelin-like 1 protein regulates myosin phosphatase-targeting subunit 1 expression during sexual development and pregnancy. The Journal of biological chemistry 285, 29357–29366. [PubMed: 20634291]

Meder D, Shevchenko A, Simons K, and Fullekrug J (2005). Gp135/podocalyxin and NHERF-2 participate in the formation of a preapical domain during polarization of MDCK cells. The Journal of cell biology 168, 303–313. [PubMed: 15642748]

Murali M, and MacDonald JA (2018). Smoothelins and the Control of Muscle Contractility. Advances in pharmacology 81, 39–78. [PubMed: 29310803]

Potter CJ, Tasic B, Russler EV, Liang L, & Luo L (2010). The Q system: a repressible binary system for transgene expression, lineage tracing, and mosaic analysis. Cell, 141(3), 536–548. [PubMed: 20434990]

Rodriguez-Fraticelli AE, Bagwell J, Bosch-Fortea M, Boncompain G, Reglero-Real N, Garcia-Leon MJ, Andres G, Toribio ML, Alonso MA, Millan J, et al. (2015). Developmental regulation of apical endocytosis controls epithelial patterning in vertebrate tubular organs. Nature cell biology 17, 241–250. [PubMed: 25706235]

Roper K (2015). Integration of cell-cell adhesion and contractile actomyosin activity during morphogenesis. Current topics in developmental biology 112, 103–127. [PubMed: 25733139]

Roux KJ, Kim DI, Raida M, and Burke B (2012). A promiscuous biotin ligase fusion protein identifies proximal and interacting proteins in mammalian cells. The Journal of cell biology 196, 801–810. [PubMed: 22412018]

Rubin DC (2007). Intestinal morphogenesis. Current opinion in gastroenterology 23, 111–114. [PubMed: 17268237]

Sahai E, and Marshall CJ (2003). Differing modes of tumour cell invasion have distinct requirements for Rho/ROCK signalling and extracellular proteolysis. Nature cell biology 5, 711–719. [PubMed: 12844144]

Srivastava J, & Barber D (2008). Actin co-sedimentation assay; for the analysis of protein binding to F-actin. Journal of visualized experiments : JoVE, (13), 690. [PubMed: 19066573]

Subedi A, Macurak M, Gee ST, Monge E, Goll MG, Potter CJ, Parsons MJ, & Halpern ME (2014). Adoption of the Q transcriptional regulatory system for zebrafish transgenesis. Methods (San Diego, Calif.), 66(3), 433–440.

Turner SR, and MacDonald JA (2014). Novel contributions of the smoothelin-like 1 protein in vascular smooth muscle contraction and its potential involvement in myogenic tone. Microcirculation 21, 249–258. [PubMed: 24267201]

Ulke-Lemee A, Ishida H, Chappellaz M, Vogel HJ, and MacDonald JA (2014). Two domains of the smoothelin-like 1 protein bind apo- and calcium-calmodulin independently. Biochimica et biophysica acta 1844, 1580–1590. [PubMed: 24905744]

Varshney GK, Pei W, LaFave MC, Idol J, Xu L, Gallardo V, Carrington B, Bishop K, Jones M, Li M, et al. (2015). High-throughput gene targeting and phenotyping in zebrafish using CRISPR/Cas9. Genome Res 25, 1030–1042. [PubMed: 26048245]

Wallace KN, Akhter S, Smith EM, Lorent K, and Pack M (2005). Intestinal growth and differentiation in zebrafish. Mechanisms of development 122, 157–173. [PubMed: 15652704]

Wallace KN, and Pack M (2003). Unique and conserved aspects of gut development in zebrafish. Developmental biology 255, 12–29. [PubMed: 12618131]

Wolf FA, Angerer P, & Theis FJ (2018). SCANPY: large-scale single-cell gene expression data analysis. Genome biology, 19(1), 15. 10.1186/s13059-017-1382-0 [PubMed: 29409532]

Zhong TP (2005). Zebrafish genetics and formation of embryonic vasculature. Current topics in developmental biology 71, 53–81. [PubMed: 16344102]

Zihni C, Vlassaks E, Terry S, Carlton J, Leung TKC, Olson M, Pichaud F, Balda MS, and Matter K (2017). An apical MRCK-driven morphogenetic pathway controls epithelial polarity. Nature cell biology 19, 1049–1060. [PubMed: 28825699]

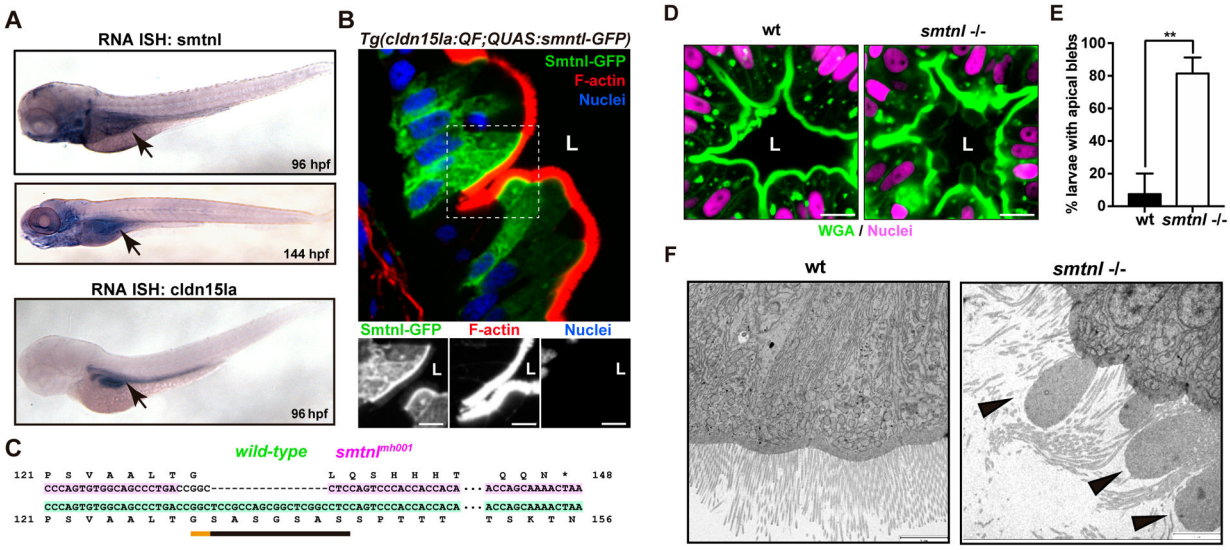

Figure 1. *Smtnl* is expressed in the enterocytes and is required for correct apical membrane organization in the zebrafish gut.

(A) In situ hybridization (ISH) of *smtnl* and gut marker *Cldn15la* DIG-labelled RNA probe at 96 – 144 hpf. Arrows indicate gut localization.

(B) Transverse section of *Tg(cldn15la:QF; QUAS:smntl-GFP)* larva anterior midgut, stained using phalloidin (which labels F-actin, in red) and DAPI (for nuclei, in blue). Scale bars 10μm (magnification 5μm).

(C) CRISPR-Cas9 generated *smtnl* mutant null allele. sgRNA were designed to target the second exon of zebrafish *smtnl* (black bar, PAM sequence in orange). Cas9-sgRNA complexes were injected at the one cell stage. After raising the founders, we cloned an allele, *smtnl*^{mh001} that harbors a null mutation.

(D) Apical membrane is disrupted in *smtnl* homozygous mutants. Larvae were fixed at 6dpf, sectioned and labelled with Alexa 488-conjugated wheat germ agglutinin (WGA), which stain lectins enriched at the apical membranes of enterocytes (green) and nuclei (magenta). L, lumen. Scale bars, 10μm.

(E) Quantification of apical blebs in *smtnl* mutant vs wild-type larvae at 144 hpf, from electron microscopy images. Values are mean ± SD (wild-type: 7.3±12.7%, *smtnl* mutant: 81.3±9.8%) sections are from 10 WT and 8 mutant fish, randomly selected, from 3 independent experiments; **, P<0.01 (Student's *t*-test).

(F) Electron microscopy of transversal sections of *smtnl* mutant larvae at 6dpf. Scale bars, 3μm.

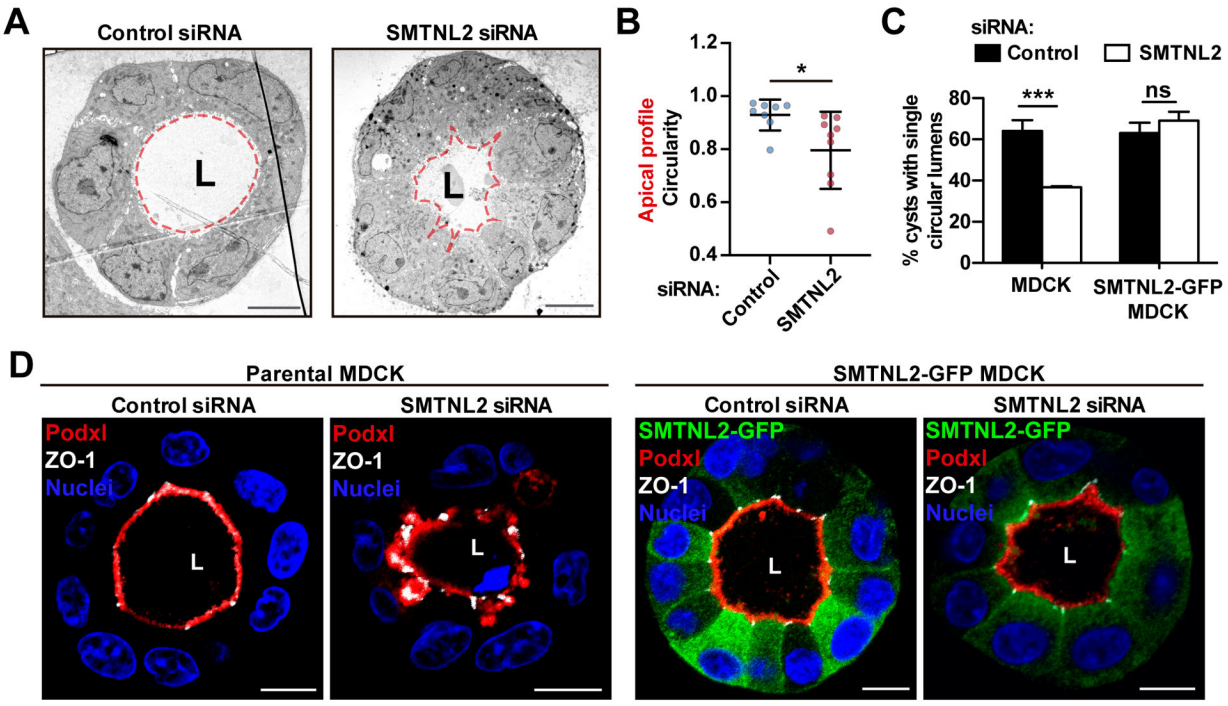

Figure 2. SMTNL2 is required for the maintenance of the cortical actomyosin structure in 3D-MDCK cells.

(A) SMTNL2-KD phenotype in MDCK cysts. MDCK cells were transfected with Control or SMTNL2-specific siRNAs and grown to form cysts at 72h. Cyst preparations were analyzed by transmission electron microscopy. Scale bars, 5μm. The apical membrane profile is marked with a red dotted line. L, lumen.

(B) Quantification of apical profile circularity. Measurements are mean ± SD percentage (Control siRNA: 0.93±0.06, SMTNL2 siRNA: 0.79±0.14, n=9 cysts). *, P<0.028 (*Welch's* t-test).

(C) Rescue of SMTNL2-KD phenotype (quantifying % of cysts with single circular lumens). Measurements are expressed as mean ± SD percentage (Control siRNA: 64±5.3%, SMTNL2 siRNA: 37±0.5%, SMTNL2-GFP Control: 63±5%, SMTNL2-GFP SMTNL2 siRNA: 69±4.3%). n = 3 independent transfection experiments; ***, P<0.001, ns, not significant (*Paired t*-test).

(D) Apical F-actin concentration during epithelial morphogenesis. MDCK cells were grown in 3D (top) or 2D (bottom) for up to 120h, fixed at different time points and stained with Phalloidin-FITC (green) and DAPI (blue). For 2D images, a cross section of a z-stack (apical to basal) is shown.

(E) Quantification of F-actin mean fluorescence intensity (MFI) apical/basolateral ratio for the experiment in (a). ***, P<0.001 (Unpaired t-test).

(F) Analysis of SMTNL2 expression in 2D vs. 3D at different time points (from 24h to 120h) by RT-qPCR. Results are mean ± SD relative to 24h 2D and normalized with Hprt1. n=3; *, P < 0.05; ** P < 0.01 (Unpaired t-test).

(G) SMTNL2 localization in MDCK cysts. SMTNL2–GFP stable cells were grown to form cysts at 72h. MDCK cysts were fixed and labeled with Phalloidin, to stain F-actin (magenta), and DAPI (blue). Scale bars 10μm.

(H) Recombinant fragments of SMTNL2 produced in E.coli. The structure of SMTNL2 was predicted to contain a coiled-coil N-terminal region, a central complex disordered region (CR) and a C-terminal globular calponin homology domain.

(I) In vitro F-actin binding capacity of full-length (FL) SMTNL2 or SMTNL2 fragments (using BSA as a control). Actin was polymerized in vitro in the presence of recombinant purified SMTNL2 fragments, and ultracentrifuged to precipitate the F-actin filaments. S, soluble fraction. I, insoluble (precipitated) fraction. Fractions were analyzed by electrophoresis and Coomasie gel stain. ****, P<0.0001 (*Unpaired* t-test).

(J) Representative images showing abnormal lumen phenotype in SMTNL2 siRNA cysts. Control and SMTNL2 siRNA cysts were grown up to 72h and labeled with Phalloidin to quantify F-actin intensity.

(K) Measurement of fraction of apical over total F-actin intensity. Plot shows individual cyst measurements (Control siRNA 48h: 0.61±0.09, n=30; SMTNL2 siRNA 48h: 0.62±0.11, Control siRNA 72h: 0.61±0.07, n=23; SMTNL2 siRNA 72h: 0.38±0.12, n=19). ****, P<0.0001 (Unpaired t-test)

(L) Turnover of apical actin in control and SMTNL2 siRNA cysts. MDCK cysts constitutively expressing PA-GFP-Actin were imaged by live confocal microscopy. Apical PA-GFP-Actin was activated with a pulse of UV light, and PA-GFP decay was measured over time for 10 min. Data represent mean GFP integrated density ±SD of n=10 cysts per treatment. Curves were fit using a one-phase decay model (non-linear regression). Extra sum-of-squares F test P < 0.0001.

(M) High SMTNL2 overexpression induces contractile basal blebs. MDCK and SMTNL2-GFP overexpressing cysts were grown up to 72h and stained for anti-pMLC (red), Phalloidin (magenta) and DAPI (blue). Two representative cysts are shown from 3 different experiments. The confocal plane selected for imaging was not the central plane. Magnification scale bars, 4μm. Scale bars, 10μm.

(N) Quantification of cysts with basal blebs. Measurements are expressed as mean ± SD percentage of total cysts (mock: 30%±0.13; SMTNL2-GFP: 85%±0.04, n=3 independent experiments). **, P<0.01 (Unpaired t-test).

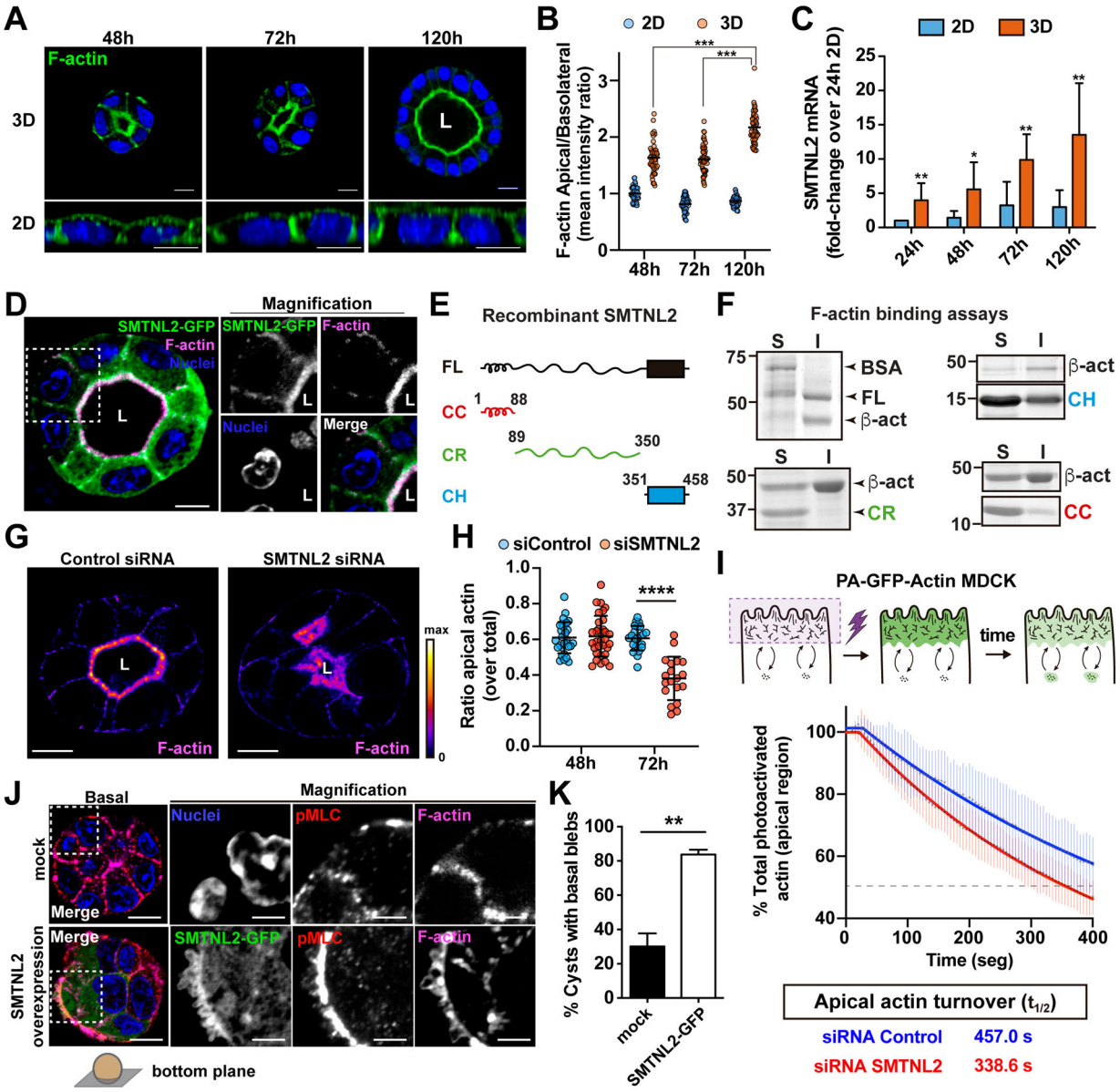

Figure 3. SMTNL2 forms part of an apical network of actin regulators.

(A) STRING plot of SMTNL2 interactome identified in the bioID assay. Thicker connecting lines represent a lower False Discovery Rate (FDR) in STRING analysis (higher confidence). Proteins are colored based on functional categories. Green, cell junctions. Purple, actin cytoskeleton. Pink, intermediate filaments. Orange, kinases/signaling components. Only interconnected components (nodes with connections) are shown.

(B) EnrichR analysis of SMTNL2 interactome. Plots represent enriched terms in Gene Ontology Biological Processes (GO BP) and the human protein complex map (hu.MAP). Only the top-ranked terms are labeled.

(C) CTTN-GFP and CORO1B-GFP localize apically with SMTNL2-Cherry. MDCK double stable cell lines expressing SMTNL2-Cherry and CTTN-GFP or CORO1B-GFP were grown

to form cysts and analyzed at 72h by confocal microscopy. Scale bars, 10μm (magnification 5μm). L, Lumen.

(D) Coimmunoprecipitation of CTTN-GFP or CORO1B-GFP and SMTNL2-Cherry. Western blots are representative of three independent experiments.

(E) Coimmunoprecipitation of Arp2 and SMTNL2 using wild-type, phosphomimetic (S2D) or phospho-dead (S2A) mutants of CORO1B-GFP. Western blots are representative of three independent experiments.

(**F)** Pulldown using different domains of His-tagged SMTNL2. His-tagged SMTNL2 fragments were incubated with lysates of CORO1B-GFP (top) or CTTN-GFP (bottom) cells, and bound to Ni-NTA beads. Western blots are representative of four independent experiments.

(G) Quantification of pulldown Western-blots in (F) (integrated density, normalized by input). Results are mean ± S.D. from four independent experiments.

(H) Quantification of coimmunoprecipitation of wild-type or ΔCC mutant SMTNL2 with CORO1B-GFP. Data are mean ± SD fraction of ΔCC SMTNL2 bound to CORO1B, normalized by the amount of FL SMTNL2 protein precipitated (0.35±0.14, n=3). *, P=0.0142 (one-sample t-test).

(I) Coimmunoprecipitation of wild-type or ΔCC mutant SMTNL2 with CORO1B-GFP. Western blots are representative of three independent experiments.

(J) SMTNL2 siRNA phenotype rescue with ΔCC SMTNL2 mutants. MDCK cells expressing ΔCC mutant SMTNL2-GFP were transfected with Control or SMTNL2-targeting siRNA and grown as cysts for 72h. Cysts were stained with Phalloidin (red) and DAPI (blue), and analyzed by confocal microscopy. Arrowhead point to abnormal apical membrane structures apparent only in SMTNL2-KD cysts.

(K) Quantification of phenotype rescue using wild-type or ΔCC mutant SMTNL2. Data are mean ± SD percentage of cysts with single circular lumens (parental Control siRNA = 80±8.88%, parental SMTNL2 siRNA = 59±7.81%, FL-SMTNL2 Control siRNA = 84±10.54%, FL-SMTNL2 SMTNL2 siRNA = 79±3.61%, ΔCC-SMTNL2 Control siRNA = 87±3.61%, ΔCC-SMTNL2 SMTNL2 siRNA = 70.33±9.3%, n=3 independent experiments).*, $P<0.05$; ns, non-significant (two-way ANOVA with Holm-Sidak correction for multiple comparisons).

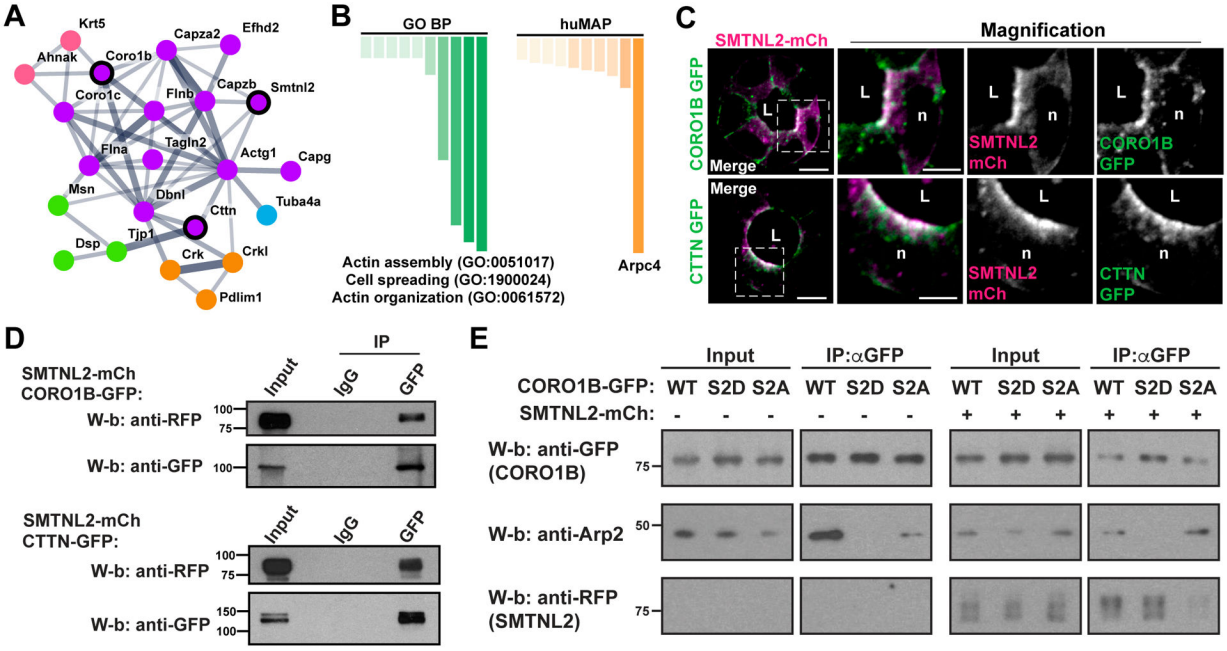

Figure 4. SMTNL2 limits CORO1B activity to maintain the normal epithelial shape.

(A) Effect of SMTNL2-GFP, CORO1B-GFP or CTTN-GFP overexpression on lumen formation at 72h. MDCK cysts were fixed, labeled with anti-Podxl (red) and DAPI (blue), and anayzed by confocal microscopy. Scale bars, 5μm.

(B) Quantification of percentage of cysts with normal lumens in cells stably expressing SMTNL2-GFP, CORO1B-GFP and CTTN-GFP vs. mock MDCK cells (mock: 64±5.3%, SMTNL2-GFP: 63±5%, CTTN-GFP: 65.6±8.7% CORO1B-GFP: 8±1.5%). All values are mean ± SD from three different experiments (n ≥ 100 cysts/experiment). ***, P<0.0001, ns, not significant.

(C) Phenotype rescue using ectopic SMTNL2 expression on CORO1B-GFP overexpressing cysts. CORO1B-GFP cells were transfected with SMTNL2-mCherry, grown as cysts for 72h and analyzed by confocal microscopy. Scale bars, 5μm.

(D) Quantifications of phenotype rescue in (C). Values are mean ± SD from three different experiments (n ≥ 100 cysts/experiment; ***, P<0.001.

(E) Phenotype rescue of SMTNL2 siRNA using ectopic CTTN-GFP overexpression. WT or CTTN–GFP cells were transfected with Control or SMTNL2-specific siRNAs and grown as cysts for 72h. Cysts were fixed, labelled with Phalloidin (red), DAPI (blue) and analyzed by confocal microscopy. Scale bars, 5μm.

(F) Quantifications of percentage of cysts with single circular lumens (Control siRNA CTTN-GFP: 58±21.8%, SMTNL2 siRNA CTTN-GFP: 63.7±5%). All values are mean ± SD from three different experiments (n ≥ 100 cysts/experiment). ***, P<0.0001, ns, not significant.

(G) Effect of Arp2/3 inhibitor CK666 on epithelial morphogenesis. Arp2/3 inhibitor and control treated SMTNL2-GFP cysts were fixed at 72h and stained with Phalloidin (red) and DAPI (blue), and analyzed by confocal microscopy. Scale bars, 5μm.

(H) Quantification of normal lumen formation in wildtype and SMTNL2-GFP cysts upon Arp2/3 inhibition at 72h. Measurements are mean ± SD percentage of all cysts (at 72h, WT: 34.0±6.7%, SMTNL2-GFP: 32.3±5.6%). n = 3 (n ≥ 100 cysts (or cells)/experiment). ns, non-significant. (*Unpaired t*-test)

(I) Model. SMTNL2 is induced during epithelial maturation to restrict CORO1B inhibition of Arp/3, stabilizing the F-actin in the apical cortex.

(J) Without SMTNL2 (in immature epithelia, or upon SMTNL2-KD), CORO1B activity prevails. While CORO1B is likely required for early epithelial remodelling, its excess is detrimental to apical cortex maturation and the final epithelial shape.

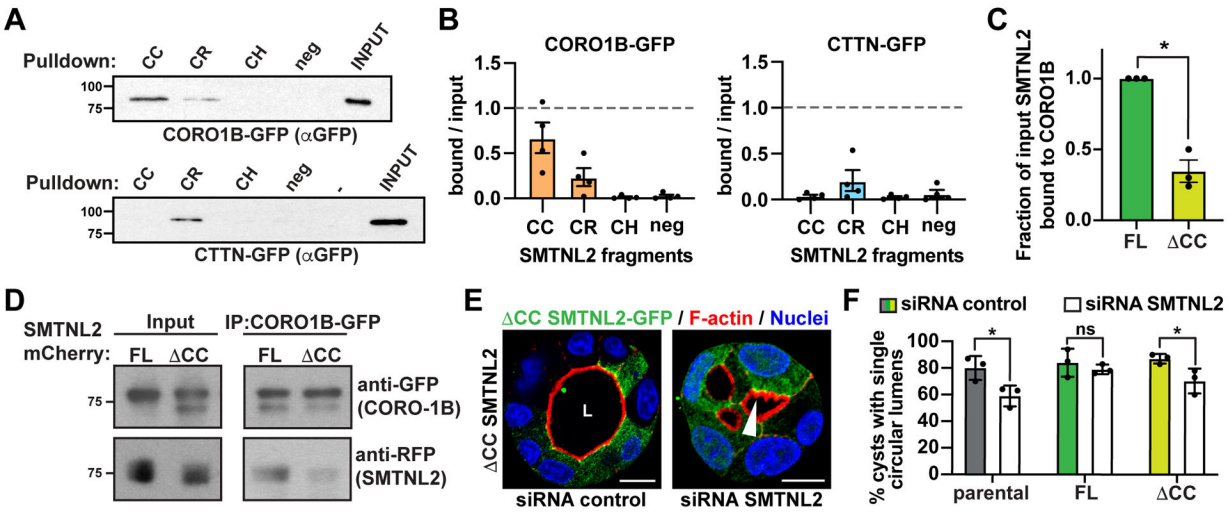

Figure 5. SMTNL2 Sequesters Phospho-CORO1B through the CC Region to Prevent Arp2/3 Inactivation SMTNL2 Sequesters Phospho-CORO1B through the CC Region to Prevent Arp2/3 Inactivation

(A) Pull-down using different domains of His-tagged SMTNL2. His-tagged SMTNL2 fragments were incubated with lysates of CORO1B-GFP (top) or CTTN-GFP (bottom) cells and bound to Ni-NTA beads. Western blots are representative of four independent experiments.

(B) Quantification of pull-down western blots in (F) (integrated density, normalized by input). Results are mean ± SD from four independent experiments.

(C) Quantification of coimmunoprecipitation of wild-type or ΔCC mutant SMTNL2 with CORO1B-GFP. Plots show the mean ± SD fraction of ΔCC SMTNL2 bound to CORO1B, normalized by the amount of FL SMTNL2 protein precipitated (0.35 ± 0.14; n = 3). *p = 0.0142 (one-sample t test).

(D) Coimmunoprecipitation of wild-type or ΔCC mutant SMTNL2 with CORO1B-GFP. Western blots are representative of three independent experiments.

(E) SMTNL2 siRNA phenotype rescue with ΔCC SMTNL2 mutants. MDCK cells expressing DCC mutant SMTNL2-GFP were transfected with control or SMTNL2-targeting siRNA and grown as cysts for 72 h. Cysts were stained with phalloidin (red) and DAPI (blue) and analyzed by confocal microscopy. Arrowheads point to abnormal apical membrane structures apparent only in SMTNL2-KD cysts.

(F) Quantification of phenotype rescue using wild-type or ΔCC mutant SMTNL2. Plots show the mean ± SD percentage of cysts with single circular lumens (parental control siRNA = 80% ± 8.88%; parental SMTNL2 siRNA = 59% ± 7.81%; FL-SMTNL2 control siRNA = 84% ± 10.54%; FL-SMTNL2 SMTNL2 siRNA = 79% ± 3.61%; ΔCC-SMTNL2 control siRNA = 87% ± 3.61%; ΔCC-SMTNL2 SMTNL2 siRNA = 70.33% ± 9.3%; n = 3 independent experiments).*p < 0.05 (two-way ANOVA with Holm-Sidak correction for multiple comparisons)

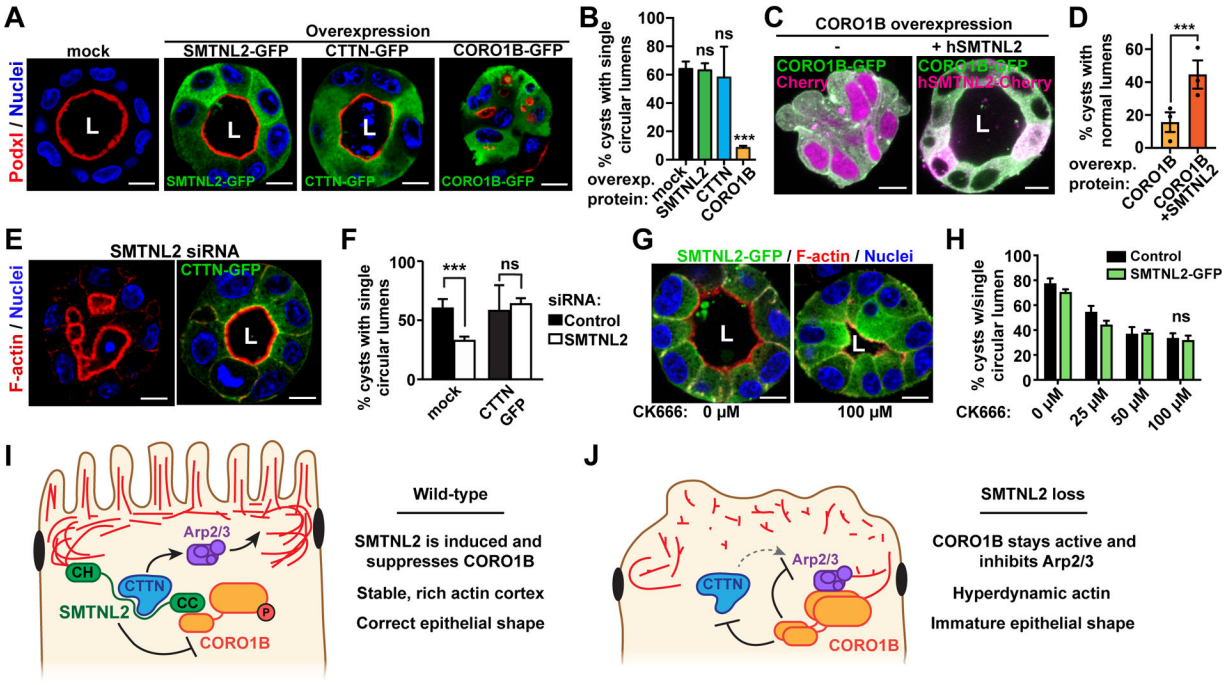

Figure 6. SMTNL2 Limits CORO1B Activity to Maintain the Normal Epithelial Shape

(A) Effect of SMTNL2-GFP, CORO1B-GFP, or CTTN-GFP overexpression on lumen formation at 72 h. MDCK cysts were fixed, labeled with anti-Podxl (red) and DAPI (blue), and analyzed by confocal microscopy. Scale bars, 5 µm.

(B) Quantification of the percentage of cysts with typical lumens in cells stably expressing SMTNL2-GFP, CORO1B-GFP, and CTTN-GFP versus mock MDCK cells (mock: 64% ± 5.3%; SMTNL2-GFP: 63% ± 5%; CTTN-GFP: 65.6% ± 8.7%; CORO1B-GFP: 8% ± 1.5%). All values are mean ± SD from three different experiments (n ≥ 100 cysts/experiment). ***p < 0.0001.

(C) Phenotype rescue using ectopic SMTNL2 expression on CORO1B-GFP-overexpressing cysts. CORO1B-GFP cells were transfected with SMTNL2-mCherry, grown as cysts for 72 h, and analyzed by confocal microscopy. Scale bars, 5 µm.

(D) Quantifications of phenotype rescue in (C). Values are mean ± SD from three different experiments (n ≥ 100 cysts/experiment; ***p < 0.001).

(E) Phenotype rescue of SMTNL2 siRNA using ectopic CTTN-GFP overexpression. WT or CTTN-GFP cells were transfected with control or SMTNL2-specific siRNAs and grown as cysts for 72 h. Cysts were fixed, labeled with phalloidin (red), DAPI (blue), and analyzed by confocal microscopy. Scale bars, 5 µm.

(F) Quantifications of the percentage of cysts with single circular lumens (control siRNA CTTN-GFP: 58% ± 21.8%; SMTNL2 siRNA CTTN-GFP: 63.7% ± 5%). All values are mean ± SD from three different experiments (n ≥ 100 cysts/experiment). ***p < 0.0001.

(G) Effect of Arp2/3 inhibitor CK666 on epithelial morphogenesis. Arp2/3 inhibitor and control-treated SMTNL2-GFP cysts were fixed at 72 h and stained with phalloidin (red) and DAPI (blue) and analyzed by confocal microscopy. Scale bars, 5 µm.

(H) Quantification of normal lumen formation in wild-type and SMTNL2-GFP cysts upon Arp2/3 inhibition at 72 h. Plots show the mean ± SD percentage of cysts with normal lumens

(at 72 h, WT: 34.0% ± 6.7%; SMTNL2-GFP: 32.3% ± 5.6%). n = 3 (n ≥ 100 cysts [or cells]/experiment). Unpaired t test.

(I) Model. SMTNL2 is induced during epithelial maturation to restrict CORO1B inhibition of Arp/3, stabilizing the F-actin in the apical cortex.

(J) Model. Without SMTNL2 (in immature epithelial or upon SMTNL2-KD), CORO1B activity prevails. Although CORO1B is likely required for early epithelial remodeling, its excess is detrimental to apical cortex maturation and the final epithelial shape.

See also Figure S5.

KEY RESOURCES TABLE

REAGENT or RESOURCE	SOURCE	IDENTIFIER
Antibodies		
gp135/Podocalyxin (3F2/D8) mouse monoclonal antibody	Developmental Studies Hybridoma Bank (University of Iowa)	Cat# 3F2/D8; RRID:AB_2618385
GAPDH (6C5) mouse monoclonal antibody	Santa Cruz Biotechnologies	Cat# sc-32233; RRID:AB_627679
β-catenin rabbit polyclonal antibody	Santa Cruz Biotechnologies	Cat# sc-7199; RRID:AB_634603
GFP (clone 7.1, clone 13.1) mouse monoclonal antibody	Millipore-Sigma (Roche)	Cat# 11814460001
GFP rabbit polyclonal antibody	Thermo Fisher Scientific	Cat# A-11122; RRID:AB_221569
myc epitope (9E10) monoclonal antibody	Millipore-Sigma (Roche)	Cat# 11667149001
RFP/DsRed rabbit polyclonal antibody	MBL International	Cat# PM005; RRID:AB_591279
Cortactin p80/85 (4F11) mouse monoclonal antibody	MERCK	Cat# 05–180
Alpha tubulin (DM1A) mouse monoclonal antibody	Millipore-Sigma	Cat# F2168, RRID:AB_476967
Phospho-Myosin Light Chain 2 rabbit polyclonal antibody	Cell Signaling Technologies	Cat# 3671; RRID:AB_330248
ZO-1 (R40.76) rat monoclonal antibody	Santa Cruz Biotechnology	Cat# sc-33725; RRID:AB_628459
Claudin-2 rabbit polyclonal antibody	Thermo Fisher Scientific	Cat# 51–6100; RRID:AB_2533911
Cleaved Caspase-3 rabbit polyclonal antibody	Cell Signaling Technologies	Cat# 9661; RRID:AB_2341188
Peroxidase-AffiniPure Donkey Anti-Rabbit IgG (H +L) polyclonal antibody	Jackson Immunoresearch	Cat# 711-035-152, RRID:AB_10015282
Peroxidase-AffiniPure Donkey Anti-Mouse IgG (H +L) polyclonal antibody	Jackson Immunoresearch	Cat# 715-035-150, RRID:AB_2340770
Penta-His epitope mouse monoclonal antibody	Qiagen	Cat# 34660; RRID:AB_2619735
Anti-Digoxigenin-AP, Fab fragments	Millipore-Sigma (Roche)	Cat# 11093274910
Dynabeads Sheep-Anti Mouse IgG	Thermo Fisher Scientific	Cat# 11031
Bacterial and Virus Strains		
BL21 Gold (DE3)	Agilent	Cat# 230130
Biological Samples		
P. pastoris X-33 yeast strain	Thermo Fisher Scientific	Cat# C18000
Chemicals, Peptides, and Recombinant Proteins		
Alexa Fluor Plus 405 Phalloidin	Thermo Fisher Scientific	Cat# A30104
Alexa Fluor 488 Phalloidin	Thermo Fisher Scientific	Cat# A12379
Alexa Fluor Plus 555 Phalloidin	Thermo Fisher Scientific	Cat# A30106
Alexa Fluor Plus 647 Phalloidin	Thermo Fisher Scientific	Cat# A30107
WGA (FITC conjugate)	Millipore-Sigma	Cat# L4895–5MG
DAPI	Thermo Fisher Scientific	Cat# 62248
6xHis-tagged human β-actin	This study	N/A
6xHis-tagged human SMTNL2	This study	N/A
GST-tagged mouse CTTN	This study	N/A
GST-tagged human CORO1B	This study	N/A

REAGENT or RESOURCE	SOURCE	IDENTIFIER
6xHis-tagged human SMTNL2 (CC fragment)	This study	N/A
6xHis-tagged human SMTNL2 (CR fragment)	This study	N/A
6xHis-tagged human SMTNL2 (CH fragment)	This study	N/A
Myosin-II inhibitor (Blebbistatin)	Millipore-Sigma	Cat# B0560–1MG
ROCK inhibitor (Y-27632)	Millipore-Sigma	Cat# SCM075
Arp2/3 inhibitor (CK-666)	Millipore-Sigma	Cat# SML0006–5MG
SpCas9 recombinant protein	New England Biolabs	Cat# M0386M
DIG RNA Labeling Mix	Millipore-Sigma (Roche)	Cat# 11277073910
Formalin solution, neutral buffered, 10%	Millipore-Sigma	Cat# HT501128–4L
UltraPure Low Melting Point Agarose	Thermo Fisher Scientific	Cat# 16520050
Fluoromount	Millipore-Sigma	Cat# F4680–25ML
D-biotin	Millipore-Sigma	Cat# 2031–1GM
Streptavidin-coated MagBeads	Genscript	Cat# L00424
KpnI	New England Biolabs	Cat# R0142S
AgeI	New England Biolabs	Cat# R0552S
SacI	New England Biolabs	Cat# R0156
Blasticidin	Thermo Fisher Scientific	Cat# A1113903
Zeocin	Thermo Fisher Scientific	Cat# R25001
G418/Geneticin	Millipore-Sigma	Cat# A1720
Coomassie brilliant blue R	Millipore-Sigma	Cat# B7920–50G
MEM	Thermo Fisher Scientific	Cat# 11095114
Fetal Bovine Serum	Thermo Fisher Scientific	Cat# 26140079
Matrigel	BD biosciences	Cat# 354234
Profinity™ IMAC Resin, Ni-charged, 10 ml	Bio-Rad	Cat# #1560131
PD-10 columns	Millipore-Sigma	Cat# GE17043501
Amicon ultracell 10 kDA cut-off membrane	Millipore-Sigma	Cat# UFC801024
Protease Inhibitor Cocktail	Millipore-Sigma	Cat# P8340–1ML
Sample Buffer, Laemmli 2× Concentrate	Millipore-Sigma	Cat# S3401–10VL
Critical Commercial Assays		
Lipofectamine 2000 transfection reagent	Thermo Fisher Scientific	Cat# 11668019
Gateway cloning LR clonase II	Thermo Fisher Scientific	Cat# 11791020
Gateway cloning BP clonase II	Thermo Fisher Scientific	Cat# 11789020
MEGAshortscript T7 Transcription Kit	Thermo Fisher Scientific	Cat# AM1354
TOPO TA Cloning Kit for Subcloning, without competent cells	Thermo Fisher Scientific	Cat# 450641
HiScribe T7 High Yield RNA Synthesis Kit	New England Biolabs	Cat# E2040S
RNeasy mini kit	Qiagen	Cat# 74104
High-Capacity RNA-to-cDNA Kit	Thermo Fisher Scientific	Cat# 4387406
MinElute Gel Extraction Kit	Qiagen	Cat# 28604
Pierce direct IP kit	Thermo Fisher Scientific	Cat# 26148

REAGENT or RESOURCE	SOURCE	IDENTIFIER
Deposited Data		
Single-cell dataset of mouse organogenesis	Cao et al. 2019 (https://doi.org/10.1038/s41586-019-0969-x)	http://atlas.gs.washington.edu/mouse-rna GEO: GSE119945
Experimental Models: Cell Lines		
MDCK type 2 (MDCK-II)	ECACC	Cat# 00062107
HEK 293T	Not validated	N/A
SMTNL2-GFP MDCK	This study	N/A
SMTNL2-mCherry MDCK	This study	N/A
GFP-CTTN MDCK	This study	N/A
mEmerald-CORO1B MDCK	This study	N/A
GFP-TAGLN2 MDCK	This study	N/A
ΔCC SMTNL2-GFP MDCK	This study	N/A
Experimental Models: Organisms/Strains		
Zebrafish: wild-type AB strain	D. Gilmour lab	N/A
Zebrafish: *smtnl* ^{mh001}	This study	N/A
Zebrafish: *Tg(Cldn15la:QF)*	M. Bagnat lab	N/A
Oligonucleotides		
See Table S1 for qPCR primers	N/A	N/A
Recombinant DNA		
Human TAGNL2 GFP plasmid	gift from Dr. Chang Duk-Jun (Gwangju Institute of Science and Technology, South Korea)	N/A
pEGFP-C1 SMTNL2	This study	N/A
pCMV Human SMTNL2-myc/myc-birA	This study	N/A
pTol2-QUAS:*smtnl*-GFP	This study	N/A
pEmerald-CORO1B-N-10	Addgene (gift from M. Davidson)	Cat# 54050
pGFP-CTTN	Addgene (gift from K. Yamada)	Cat# 26722
pmCherry-C1 SMTNL2	This study	N/A
pCMV/Bsd (pBlastR)	Thermo Fisher Scientific	Cat# V51020
pEGFP-C1 ΔCC-SMTNL2	This study	N/A
pGEM-T Easy human ACTB	This study	N/A
pPICZA human ACTB	This study	N/A
Software and Algorithms		
GeneMapper Software 5	Thermofisher Scientific	Cat# 4475073; RRID:SCR_014290
Fiji (ImageJ v2.1.0)	http://fiji.sc	RRID:SCR_002285
Zen	Zeiss (https://www.zeiss.com/microscopy/int/products/microscope-software/zen.html)	RRID:SCR_013672
Scanpy (v1.4.6)	https://github.com/theislab/scanpy	RRID:SCR_018139
Rstudio (v1.3)	https://rstudio.com/	RRID:SCR_000432
Enrichr	https://maayanlab.cloud/Enrichr/	RRID:SCR_001575
GOrilla	http://cbl-gorilla.cs.technion.ac.il/	RRID:SCR_006848

REAGENT or RESOURCE	SOURCE	IDENTIFIER
STRING	http://string.embl.de	RRID:SCR_005223